

# Gravity Loading Countermeasures Skinsuit (GLCS)

Load adjustment and stretch/load monitoring system



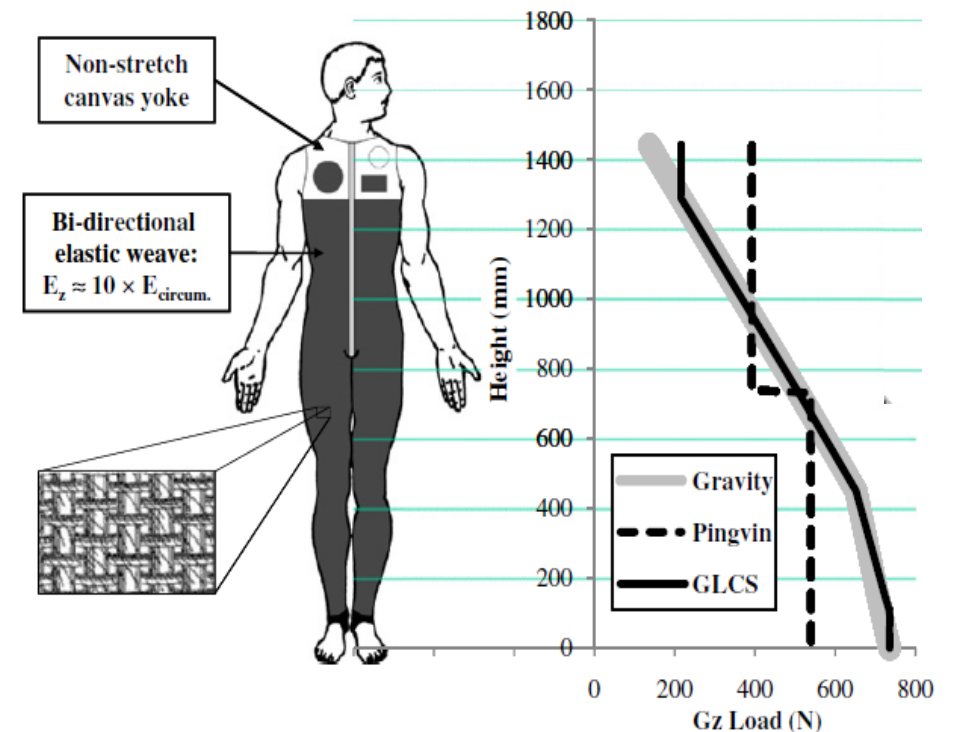
Astronaut: Andreas Mogensen (September 2015)

Inventor: James Waldie of the Royal Melbourne Institute of Technology (RMIT)

Designer: Massachusetts Institute of Technology

Manufacturer: Dainese

Tester: King's College London & ESA



Waldie, J. M., & Newman, D. J. (2011). A gravity loading countermeasure skinsuit. *Acta Astronautica*, 68(7-8), 722-730.

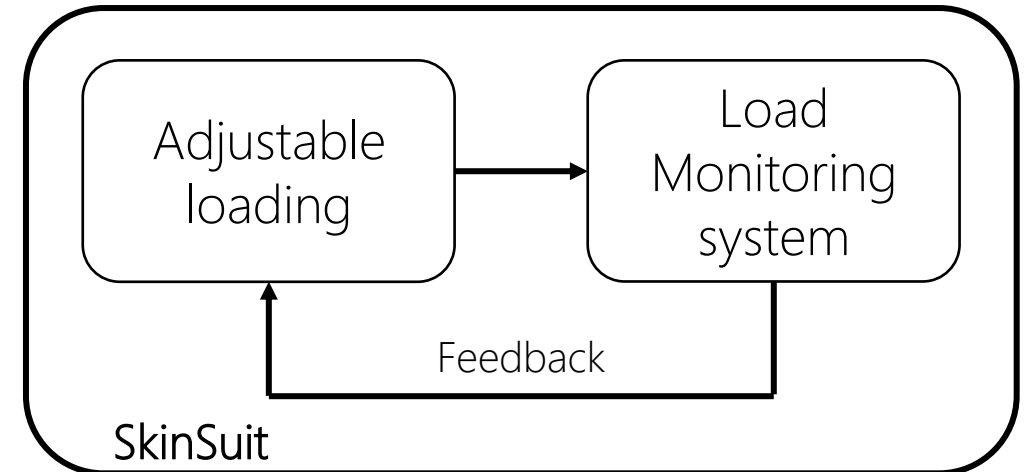
The **goal** of the **SkinSuit** is to **mimick the Earth gravity** and thus passively mitigate the deconditioning of an astronaut's body during spaceflight on ISS and bed rest conditions.

## **OBJECTIVES**

- Load adjustment and stretch/load monitoring system
- Spinal Elongation Monitoring (SEM) system

## **OUTLINES**

- Design a proof-of-concept of stretch mechanism
- Design a Load/Strech Monitoring (LSM) system
- Design a Spinal Elongation Monitoring (SEM) system with custom stretch sensor



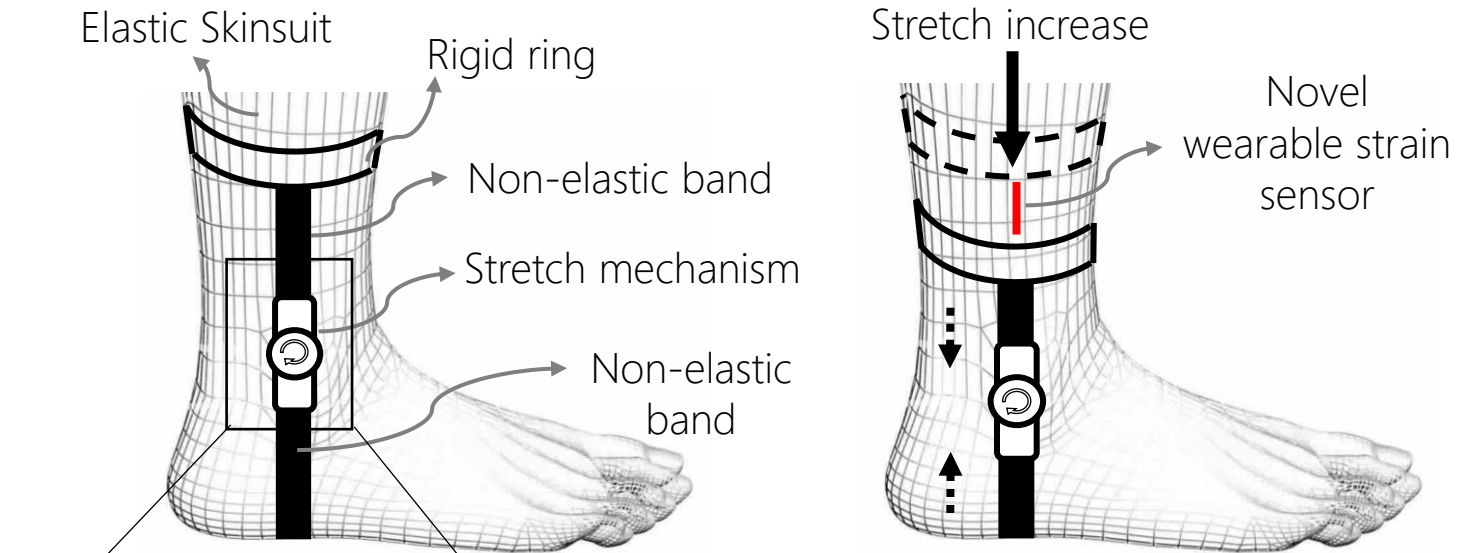
# CURRENT SOLUTION

## Disadvantages:

- Manual (2 person)
- Unintentional loosening
- No calibrated adjustment
- No monitoring loading
- Asymmetric stretch
- Uncomfortable & bulky



# SOLUTION PROPOSED



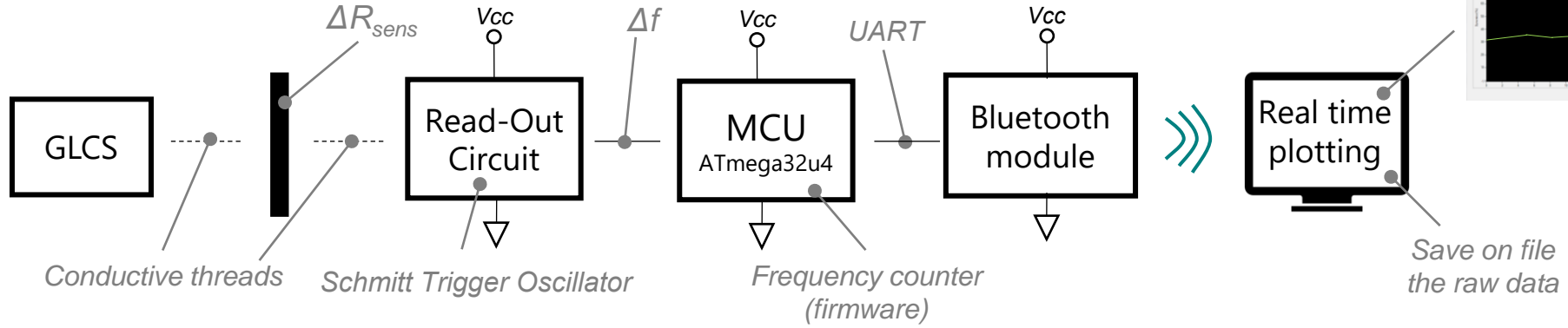
## Wearable stretch sensor

Material: Wacker ELASTOSIL R570/70 carbon conductive bi-component silicon

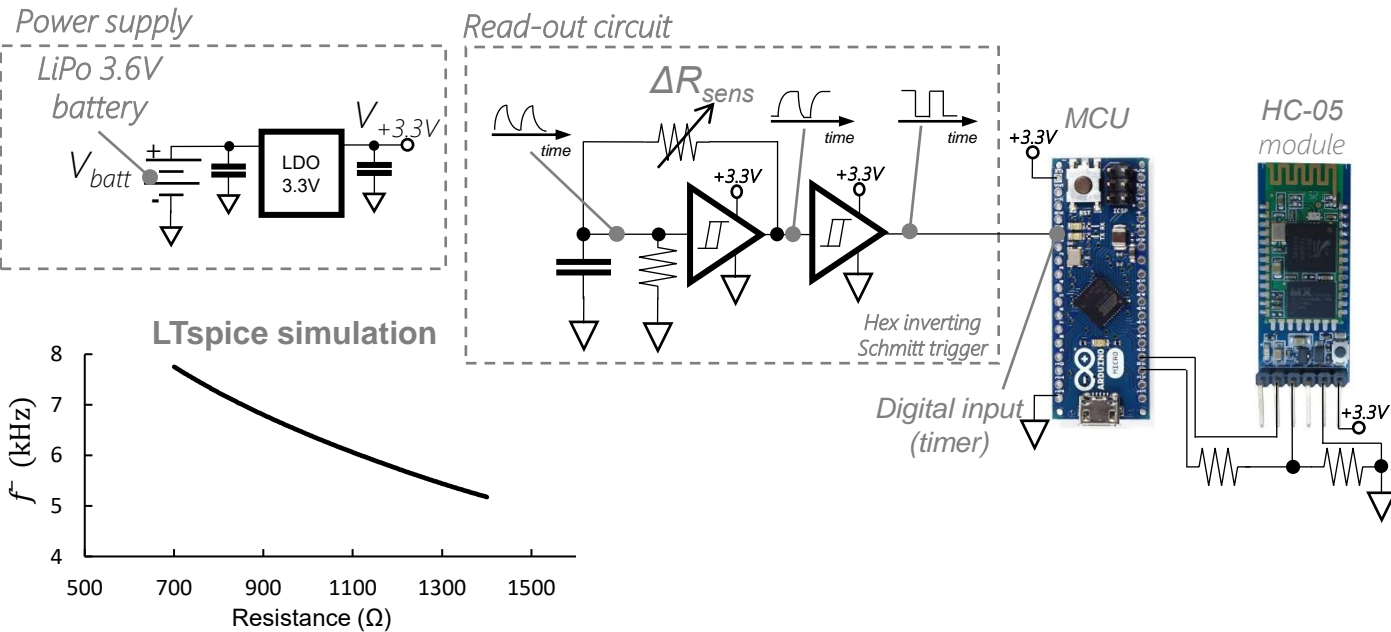
Manufacturing process: crosslinking at  $T > 170$  °C and post curing for at least 4 h at 200 °C after molding

Result: conductive silicon with piezoresistive properties

# SYSTEM ARCHITECTURE



# DEMONSTRATOR



# Gravity Loading Countermeasures Skinsuit (GLCS)

## Spinal Elongation Monitoring (SEM) system

Gravity **affects the musculoskeletal system**. In 0-g condition **the spine can elongate** up to **6.9 cm**, due to an absent of a vertical compression that change the hydrostatic pressure gradients inducing **intervertebral disc expansion**.

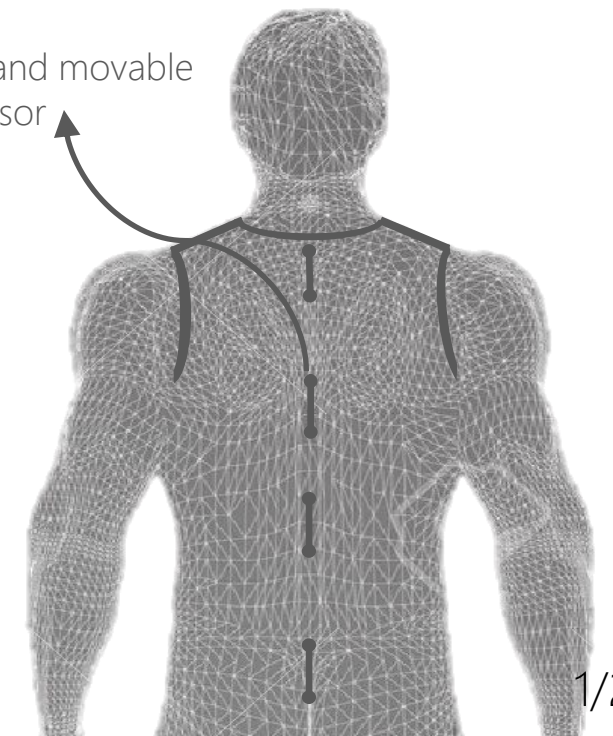
WHAT

- **Consequences:** chronic back pain, incorrect posture and risk to abort long term mission
- **Current solution:** periodic height measurement with a stadiometer or a mark on the internal wall of the space module

### Objectives

Selective evaluation of the spinal length variation (with and without the Skinsuit) designing a stretchable and comfortable wireless sensor

Wearable and movable stretch sensor



# PRELIMINARY

## CONSIDERATION

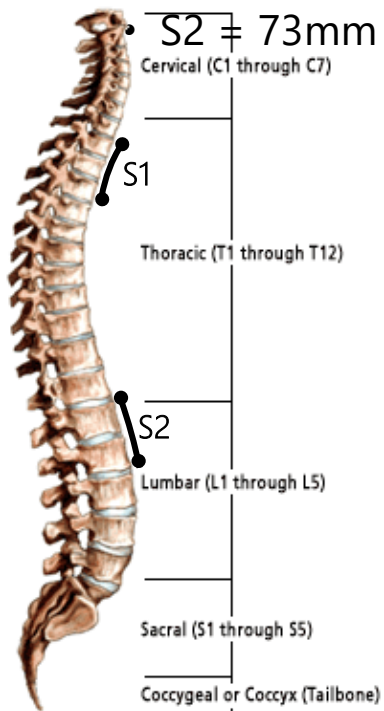
Sensor material selection (Wacker ELASTOSIL

R570/50)

Length of the sensors:

- S1 = 51mm T2-T4

- S2 = 73mm T12-L2



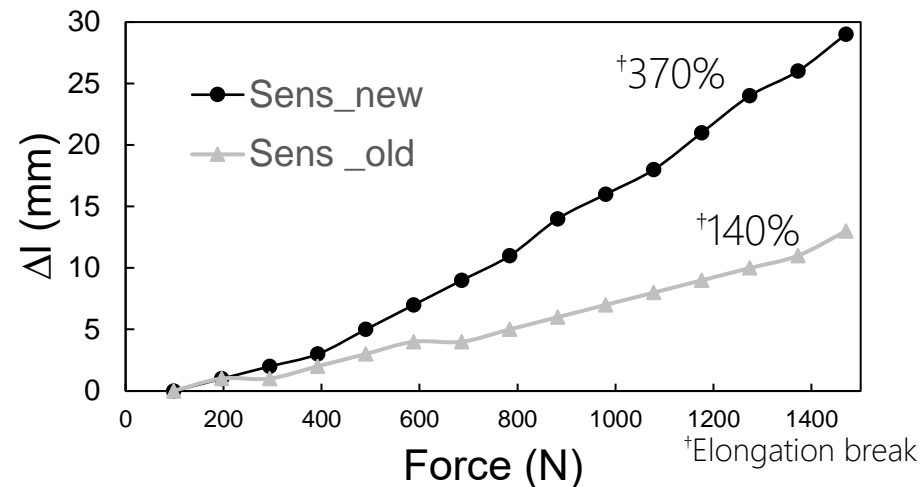
Integration of the sensor plus custom circuit to be attached on the human body



Metallic snap fastener

Sensing material

ECG electrode

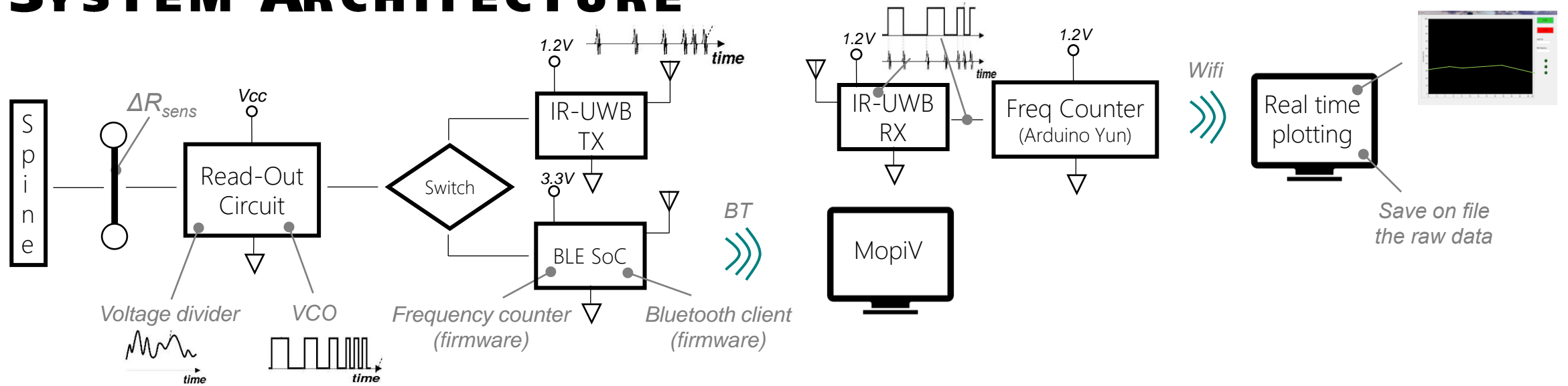


Round circuit

Circuit features:

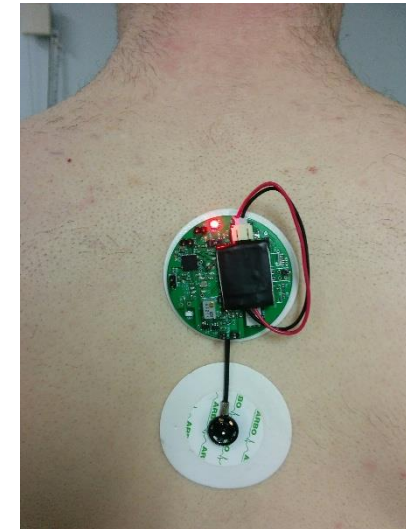
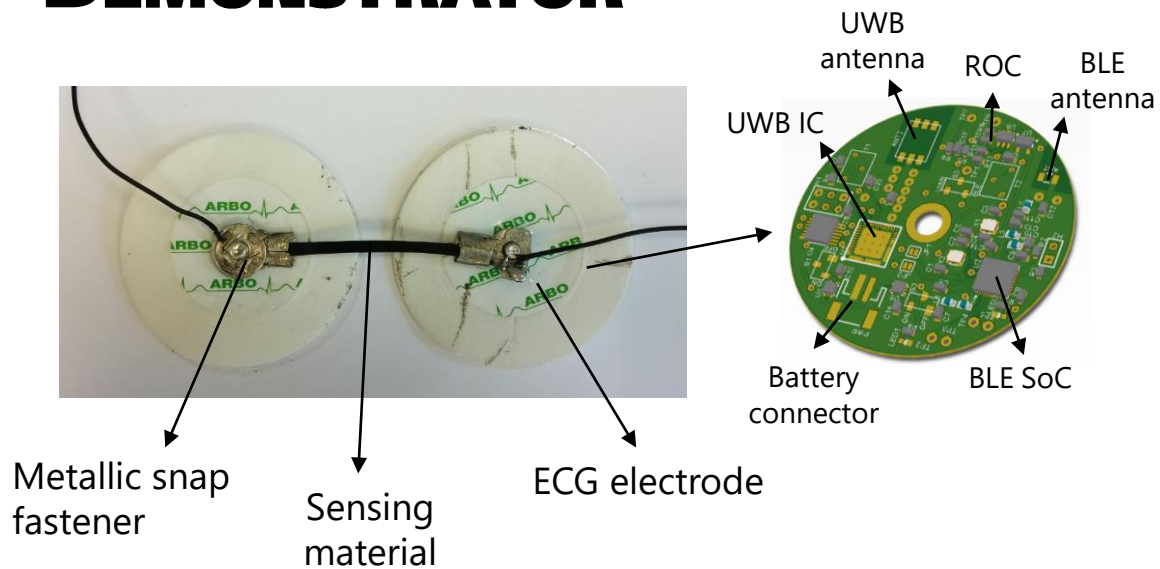
- read-out circuit
- low power data transmission (BLE and UWB)
- size  $\varnothing < 4.5$  cm
- single layer of components

# SYSTEM ARCHITECTURE



HOW

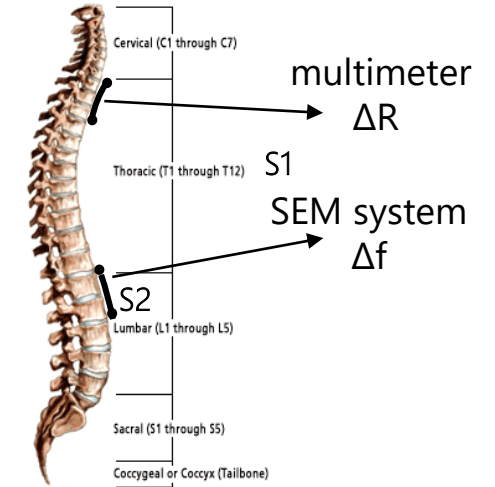
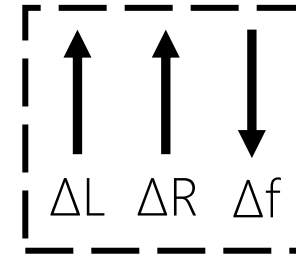
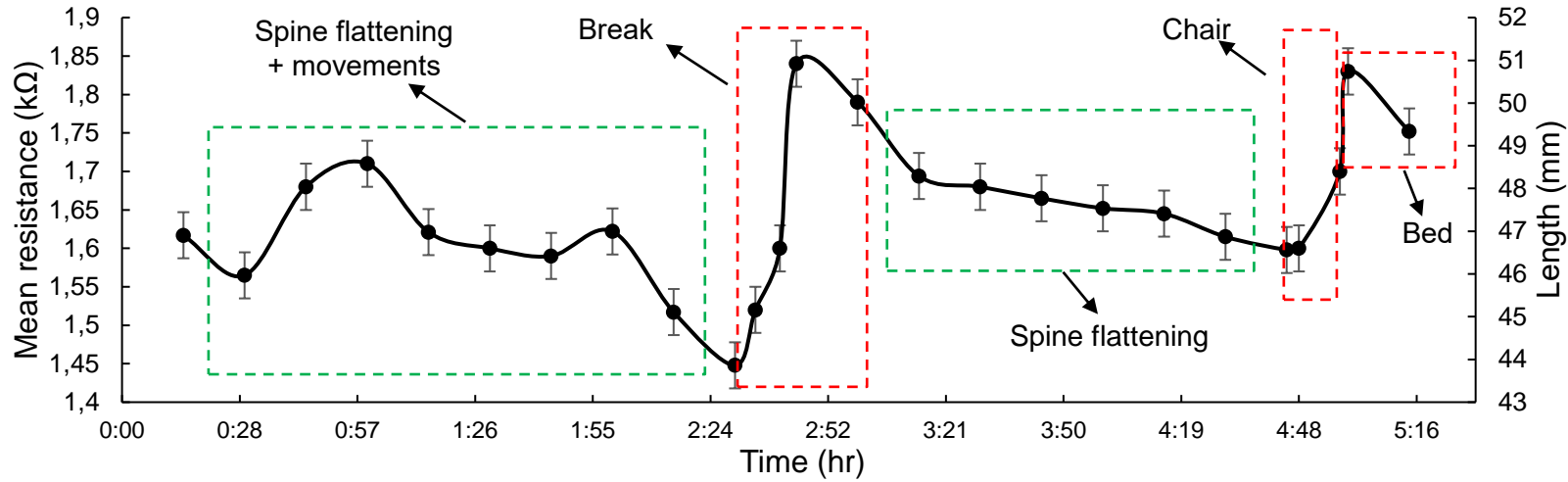
# DEMONSTRATOR



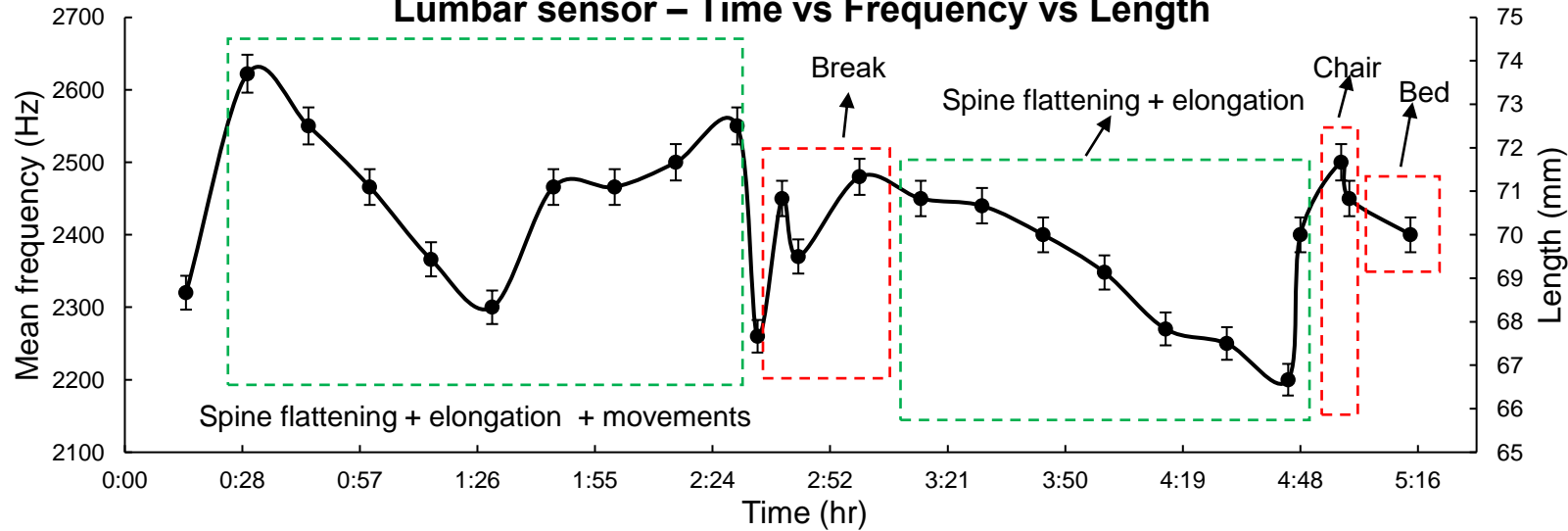
# TEST AND RESULTS

EM MONITOR

### Torax sensor - Time vs Resistance vs Length



### Lumbar sensor - Time vs Frequency vs Length



Hyper-Buoyancy Floatation (HBF)

# Publications

## PAPER IN INTERNATIONAL JOURNAL

- Stoppa, M. et al., "*Wearable electronics and smart textiles: a critical review*", Sensors, 2014, 14(7), 11957-11992;.
- Scalisi, R. G., Paleari, M., Favetto, A., Stoppa, M., et al. A. "*Inkjet printed flexible electrodes for surface electromyography.*" Organic Electronics, 2015, 18, 89-94.
- Crepaldi, M., Stoppa M., et al. "*An Analog-Mode Impulse Radio System for Ultra-Low Power Short-Range Audio Streaming.*" IEEE Transactions on Circuits and Systems I: Regular Papers, 2015, 62(12), 2886-2897.

## CHAPTER OF SCIENTIFIC BOOK

- Stoppa, M. et al, "**Testing and evaluation of wearable electronic textiles**". Lijing Wand ed., In Performance testing of textiles: methods, technology and applications. Elsevier, Langford Lane, Oxford OX5 1GB, United Kingdom, pp. 298-346.

## PROCEEDINGS OF INTERNATIONAL CONFERENCE

- Stoppa, M., et al. "*Live Demonstration: An Ultra-Low Power PFM IR-UWB System for Short-Range Audio Streaming*", International Symposium on Circuit and Systems 2015, Lisbon.
- Stoppa, M., et al., "*A Quasi-Digital Pressure/Touch Sensor Prototype for Orbital Targets Contact Event Monitoring*" International Symposium on Circuit and Systems 2016, Montreal.

# Awards

- Stoppa, M., Master Thesis *"Technological Demonstrator for a Space Medicine Wearable System"*  
**Young Investigator Award ISSBB 2012** - Italian Society for Space Biomedicine and Biotechnology
- Stoppa, M. et al. *"Wearable electronics and smart textiles: a critical review"*, Sensors, 2014, 14(7), 11957-11992;  
**Most highly cited paper published in the Sensors Journal in 2014**
- Stoppa M., PhD Dissertation *"Smart Devices and Systems for Wearable Applications"*  
**Best PhD Activity Award 2016**
- Stoppa M. and Green D.A., *"A new generation of weird-looking space suits will take us to Mars."* 2015, The Conversation (online journal)



**Award: 100K readers in 1 month**

- Invitation as speaker for the **"Future Clothing Technologies Workshop"** at the European Astronaut Center (EAC) – Cologne (Germany), September 2015.
- Selection as tester for the astronaut experiment entitled **"Effect of Tilting with LBNP on head-ward arterial, venous and intraocular pressure increases (SETI)"** at the German Aerospace Agency (DLR) – Cologne (Germany), November 2015

## Chapter 6

# Gravity Loading Countermeasures SkinSuit

Gravity has a profound effect on human evolutionary development, shaping not only its mechanical dynamics but also its supporting mechanisms (White and Averner, 2001; Blaber, Marçal, and Burns, 2010). Despite the use of several countermeasures, significant physiological deconditioning still occurs during long duration spaceflight. The effects on the musculoskeletal system are perhaps the greatest challenge to solve primarily due to the absence of loading in microgravity. Seeking new countermeasures is an on-going priority for long-term space mission programs (Convertino, 1996). Wearable technologies are significant relevant in space exploration research (Cadogan, 2015), as demonstrated from the manifold progresses of the SpaceSuits, a complex wearable systems able to preserve the health of the astronauts during External Vehicular Activities (EVA), and to counteract the effect of the microgravity. A new generation of wearable system, Gravity Loading Countermeasure SkinSuit (GLCS), was used for the first time on the International Space Station (ISS) on September 2015 within the IRISS space mission (Vicente and Walker, 2015). It is a passive garment made with elastic materials able to provide a simulated gravity loading on the body thanks to a bidirectional weave material strain that develops loads cumulatively towards the legs (Waldie and Newman, 2011). This Chapter is focused on the research activities within the GLCS project with the objective to turn the SkinSuit from a passive into an active wearable countermeasures system and to monitor the effects of the microgravity on the spinal column, and thus length, via a novel wearable system. A background of the physiological effects on the human body due to the space environment and the State Of the Art (SoA) of the current countermeasures is presented. Then, Paragraph (6.3) details a proof of concept of an Gz-load control system, coupled with a Load Monitoring (LM) system. Following trials, the load monitoring approach, was succeeded by a superior Stretch Monitoring (SM) system was integrated within the SkinSuit. Finally, this Chapter

shall define the Spinal Elongation Monitoring (SEM) system: a proof-of-concept of the first wearable device able to measure the spinal elongation in microgravity conditions.

## 6.1 Background of the Technology

During spaceflight, the human body is subject to physiological adaptation to the microgravity conditions. Humans are well adapted to living in a 1-G environment, thus the microgravity environment of space can have profound effects on the human body.

Exposure to microgravity, whether simulated or actual, was shown to result in a reductions of the ventricular mass (Eckberg et al., 2010), blood volume (Eckberg, 2003), balance control (Reschke et al., 2009), nervous system sensitivity and reserve (Cooke and Convertino, 2007), arterial tone (Verheyden et al., 2009), bone mass (Lang et al., 2004), immune function (Baqai et al., 2009) skeletal muscle mass (Blaber, Marçal, and Burns, 2010) and lead to development of space motion sickness (Lackner and DiZio, 2006). These changes can lead to operational difficulties and health consequences, both in space and upon return to a gravitational body (including Earth or future missions to the Moon/Mars).

Some of the most profound changes occur in the musculoskeletal system. Bone is a dynamic organ that adapts to the loads under which it is placed. Due to the unloading caused by the microgravity environment during long-duration spaceflight missions, astronauts can lose up to 1-2% Bone Mineral Density (BMD) per month, concentrated in the weight-bearing areas of the skeleton, which is equivalent to the yearly losses observed in post-menopausal women (Stein, 2013; Smith et al., 2014). Astronauts in space lack the normal static loading due to standing in 1 G, but also the dynamic loads caused by impact and muscle activation during movement. Bone loss may be the most important limiting factor for long-term spaceflight, due to the risk of fracture (Bikle, Sakata, and Halloran, 2007; West, 2000).

Similarly, degradation of muscle mass, force and power have been observed (Fitts et al., 2010; Gopalakrishnan et al., 2010). Since muscle contractions are also a major source of bone loading, the loss of muscle power may accelerate bone loss. Astronauts commonly complain of back pain during initial exposure to microgravity, presumably is related to spinal elongation that occurs in the absence of gravity. In fact, approximately 50% of crewmembers reported back pain due to the spine elongation of up to 70 mm (Barratt and Pool, 2008). Spinal elongations also seen on earth after extended periods of lying down, such as during sleep, when the spine can lengthen by as much as 2-3 cm (Styf et al., 1997). Elongation of the

spine can affect the fit of space hardware custom-made for astronauts (e.g. EVA spacesuits) such as the launch and re-entry seats made for the Russian Soyuz vehicle (Wing et al., 1991).

## 6.2 Wearable Countermeasures

Health and fitness procedures and programs are required to mitigate the effects of living in microgravity, and ideally retain Earth-bound baselines. These approaches and related devices are collectively called countermeasures. For more than 50 years, countermeasure solutions have been developed and evaluated during spaceflight, including physical exercise apparatus (Convertino, 1996), nutritional supplement (Smith et al., 2005), compression/loading clothing (Stenger et al., 2010) and artificial gravity concepts (Young et al., 2001). Limitation of efficiency and impracticality of current countermeasures to microgravity for new exploration missions require a more thorough understanding of the issues and the development of new solutions (Hargens, Bhattacharya, and Schneider, 2013).

While certain pharmaceutical measures, such as bisphosphonates to prevent bone loss, are being considered, at present the only countermeasure being used to actively address physiological deconditioning is physical exercise (Cavanagh, Licata, and Rice, 2007). Recent evidence shows that current exercise programs using the Advanced Resistive Exercise Device (ARED) are more effective in preventing deconditioning than previous ones, but still exercise alone is not sufficient to completely prevent bone and muscle loss. Additionally, astronauts currently devote a significant amount of time to exercise (Smith et al., 2012), time that could be spent performing critical science or maintenance activities. The idea of a passive countermeasure suit has existed for nearly as long as human spaceflight.

Recently, the Gravity Loading Countermeasures SkinSuit (GLCS) project created a new intravehicular body suit for use as a countermeasure. As a replacement of normal intravehicular garment, it would be worn by the crewmember during daily activities, providing a constant stimulus to bone/muscle inducing a constant load on the body to mimic standing and - when integrated with other countermeasures to improve the efficiency of exercising on Earth. Furthermore, an intelligent garment of this kind would offer another tool to scientifically evaluate the effects of the Gz loading on crew health in the microgravity environment (Attias et al., 2013).



FIGURE 6.1: Russian Pingvin Suit

### 6.2.1 Penguin Suit

The Russian Penguin (Penguin) suit (Figure 6.1), developed in the 1970's by Professor Arnlod Barer, is one of the current wearable countermeasures used on the International Space Station (ISS). It was not designed to mimic gravity, but induces weight-bearing stresses on the skeleton, and resistive exercise to the muscles. It uses elastic bands attached to non-stretch anchors at the shoulders, waist, knees and feet to impose two stages of loading on the body (Kozlovskaya et al., 2015). Upper and lower body loading along the vertical axis (z-axis) are imposed by bungee cords above and below a leather belt: from the shoulder to the belt (upper body), and from the belt to the feet (lower body). The upper body can be loaded up to 40 kg, with this load transmitted to the whole body if the belt is loose. Russian Cosmonauts, however, have found it difficult to wear the suit for the recommended 8 hours a day because it is hot and uncomfortable. The Penguin Suit has poor thermal conductivity that presents significant hygiene issues since, given the fact that clothing cannot be washed in microgravity, presents a significant risk of skin infection (Ewert and Jeng, 2015). Whilst quantification of actual loading has not been published, it is stated to provide a constant load of around 400 N (Waldie and Newman, 2011).

### 6.2.2 Gravity Loading Countermeasures SkinSuit - GLCS

In an attempt to address some of these issues following the development of elastic fibre and advanced weaving technology the Gravity Loading Countermeasure SkinSuit (GLCS) (Figure 6.2), was conceived at the Massachusetts

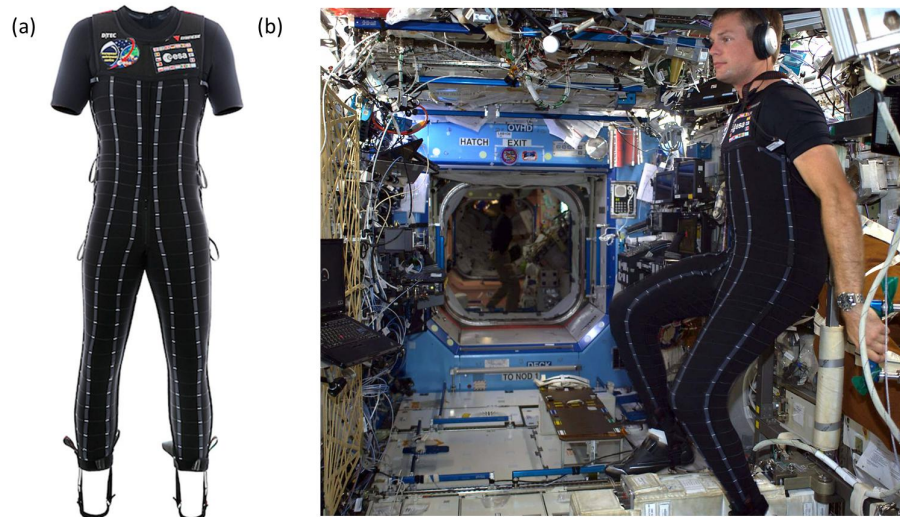


FIGURE 6.2: (a) Design of the Gravity Load Countermeasure Skin-Suit (GLCS). (b) GLCS during the IRISS space mission - astronaut ESA A. Mogensen

Institute of Technology (MIT). SkinSuit technology has the potential to provide low mass, low volume and zero-power usage. The minimal time consumption potentially improving both well characterised musculoskeletal de-conditioning. However, it may reduce potentially injury-risk inducing lower back pain.

The GLCS uses a concept similar to the Penguin suit: a passive garment using elastic materials to provide axial loading to the body. The main difference lies in the fact that the GLCS seeks to improve comfort and to mimic more closely gravitational loading by incrementally increasing the loading from the head to the feet. Figure 6.3 shows the loading profile achieved by a non-uniform stretching of the elastic material, gradually increasing the tension in the vertical direction. The circumferential compression caused by the horizontal fibers anchors the suit to the body by utilizing the friction force between the suit material and the skin. This allows the suit to achieve a portion of the bodyweight loading at the soles of the feet, without the entire load being carried on the shoulders. An initial prototype of the suit was tested on a parabolic flight campaign, and characterized for wearability and comfort (Kendrick and Newman, 2014).

The suit material is a bi-directional elastic weave to achieve the different longitudinal and lateral tensile requirements (Waldie and Newman, 2011). Fibers are oriented with high stiffness or along the  $z$ -axis,  $E_z$ , so that substantial bodyweight forces can be created without over-stretching the weave, particularly in the lower body. Conversely, low module fibres are used circumferentially,  $E_{circum}$ , to facilitate easy donning/doffing, and so

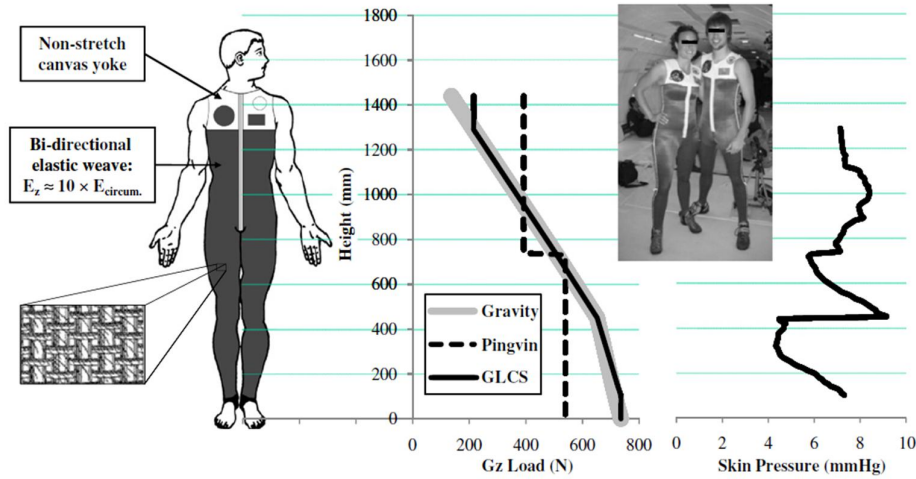


FIGURE 6.3: Gravity loading countermeasure skinSuit (GLCS) with loading regime and skin pressure

that the tension (and hence applied skin pressure) would not vary significantly due to changes in body shape. In recent versions of the SkinSuit, developed by James Waldie (RMIT University), European Space Agency (ESA) and King's College London, arrestor ribbons aligned vertically prevent over-extension of any specific 4 cm section of material. Skin pressure,  $p$ , is equal to the force  $N$  divided by area  $A$ , but is also described by the hoop tension equation 6.1 for a thin walled cylinder

$$p = \frac{N}{A} = \frac{T}{r} \quad (6.1)$$

where  $T$  is the circumferential material tension and  $r$  is the body segment radius. The height of each stage of the skinSuit,  $h$ , is equal to the spacing between the circumferential fibres of the material, and Area  $A$  under each stage is therefore equal to the local body circumference multiplied by the stage height, or  $2\pi r h$ . Using this data and Eq. 6.1 to solve circumferential material tension becomes

$$p = \frac{Nr}{A} = \frac{N}{2\pi h} \quad (6.2)$$

The resistance of the suit to sliding up and down is related to friction forces  $F$ , equal to the coefficient of friction between the elastic and the skin  $\mu$  multiplied by the normal force  $N$ . For the GLCS,  $F$  represents the axial force trying to displace the suit, and is the difference in loading above and below the stage.  $F$  is prescribed as a rate of change in the 1-g loading regime, rather than the absolute loading at the z-coordinate. The normal force  $N$  is the force applied by the material on the skin compression,  $N$ ,

required to prevent the stage slipping under the force  $F$ . Therefore the tension yields is expressed by the Eq. 6.3

$$T = \frac{F}{2\pi h\mu} \quad (6.3)$$

where, following the Eq. 6.1, the skin pressure is

$$p = \frac{F}{2r\pi h\mu} \quad (6.4)$$

The Mark VI SkinSuit was studied during the IRISS space mission (2-12 September 2015) performed by ESA astronaut Andreas Mogensen in which the objective were:

- to evaluate the ability of the SkinSuit to counteract spine elongation and reduce, or even prevent, lower-back pain - It was assessed through frequent measurements of Andreas's height as well as a pain and questionnaire;
- to measure the +Gz load that SkinSuit provides whilst on the Space Station using NASA's Force Shoes - The plan was to measure the load in three standard postures to evaluate the experience by Andreas during a day on the ISS. However this task was not completed;
- to evaluate operational considerations, in particular in regard to hygiene (by collecting microbiological skin swabs), comfort, temperature regulation and range of motion (by questionnaires);
- to evaluate the effect of wearing the SkinSuit while exercising on the ISS CEVIS bicycle exercise machine.

Notwithstanding the final goal to mimic the Gz force on the musculoskeletal system with a gradual force distribution. One of the current limit of the GLCS is the inability to control the loading. Each GLCS is designed and tailored personally for each subject. Since the zero-g effects start to appear and to get worse, in a different manner for each subject and with different timing during a spaceflight mission, a load adjustment mechanism would allow to develop an *adaptable* system able to customize the countermeasure effects. Thus, the objectives of this Chapter are:

- to provide a Gz-load adjustment system;
- to give the chance to adjust the load according to different gravity condition (0-g, Moon or Mars gravity);
- to monitor the load variation;
- to investigate the balance between GLCS loading and comfort.

Moreover, the GLCS does not allow to monitor the g loading status over time, since the wearable system is entirely passive and it is designed to produce the maximum load available, following the anatomic measurements of the subjects. This requirement begins to be significant if the GLCS is able to adapt the g-loading according to the needs.

This Chapter defines a proof-of-concept of a adjustable Gz-load system and a wearable Load/Stretch Monitoring (L/SM) designed and characterized in order to obtain a real-time measure of the load and to titrate loading concurrently. As access to GLCS is limited, to test and to validate the adjustable load mechanism, a GLCS simulator was developed according to the original properties of the suit in terms of performance and mechanical properties.

### **6.3 Load Adjustment and Monitoring System for the GLCS**

The current MK VI GLCS is designed to achieve around the 20-25% of the subject's body weight. Previous versions (Mark I, II, III) achieved higher loading but discomfort was significant. Exploiting the elastic properties of the SkinSuit material and its design, the stretch level can be adapted, increasing or decreasing the Gz-load. Furthermore, this Gz-load variation has to be monitored with a wearable system embedded within the GLCS.

In the first part of this section, a proof-of-concept of a load adjustment mechanism and a Load Monitoring (LM) system, integrated within the lower body GLCS simulator, are presented:

- definition of the project requirements;
- design of the load adjustment mechanism;
- design of the lower body GLCS simulator - tests and results;
- implementation of the the load adjustment mechanism with the lower body GLCS simulator - test and results;
- design and implementation of the LM system - test and results of the overall system;

Following the results obtained during the previous experiment, the second part of the section presents a more reliable solution to monitor the Gz-load variation of the GLCS, exploiting the stretch properties of the suit material. The Stretch Monitoring (SM) system designed is based on a custom and wearable stretch sensor coupled with a wireless read-out circuit. On the basis of the results obtained the SM system has been selected to be integrated within the SkinSuit for the future field testing.

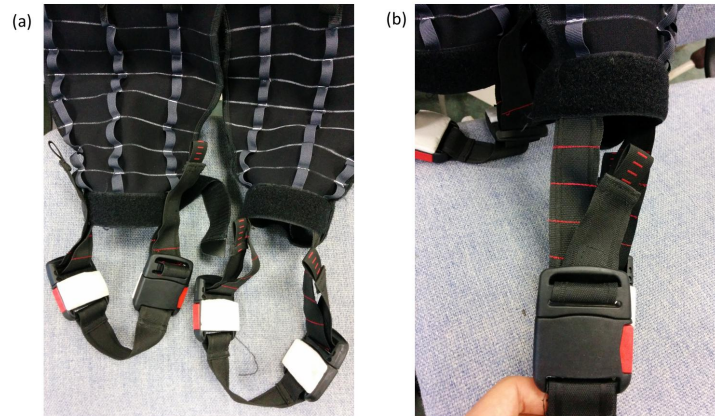


FIGURE 6.4: Gravity Load Countermeasure SkinSuit lock mechanism. (a) Lower part of the SkinSuit. (b) Detail of the lock mechanism

### 6.3.1 Requirements Definition

The structure of the SkinSuit can be sub-divided into three main sections:

- non-stretchable canvas yoke around the shoulders;
- gradual stretchable material from the chest to the ankles;
- non-stretchable stirrups wrapped around the sole of the foot.

The main feature of the GLCS, in comparison with the Penguin Suit, is the loading profile obtained via non-uniform stretching of the elastic material, which gradually increases the tension along the vertical direction, with an analogue path of the gravity force profile. This important aspect has not to be altered with the implementation of a new mechanism or other system. For this reason, the GLCS' portion candidate to be adapted with the new mechanism is the bottom part, where the non-stretchable stirrups are connected through buckle clips in the rest of the suit. Figure 6.4 shows the current lock mechanism used in the GLCS Mark V. Following interviews with some ESA members involved in the GLCS project, Table 6.1 summarizes the advantages and disadvantages of the existing system.

The solution proposed aims to replace the buckle clips with a wearable mechanism able to change the length of the stirrups and then the stretch (or load) level produced by the SkinSuit. In order to obtain a balanced load, a couple of mechanisms have to be used for each ankle. Figure 6.5 shows the working principle of the load adjustment system.

The load adjustment device has to maintain the benefits of the current system whilst allowing a fine control of the SkinSuit's  $G_z$ -load. To enhance comfort, the system has to be compliant with the body shape, in particular the ankle anatomy and ensuring a reliable connection with the rest

TABLE 6.1: Advantages and disadvantages of the current design.

<b>Advantages</b>	<ul style="list-style-type: none"> <li>- easy and simple implementation;</li> <li>- rapid lock and unlock;</li> <li>- always integration with Force-shoes.</li> </ul>
<b>Disadvantages</b>	<ul style="list-style-type: none"> <li>- no-calibrated adjustment;</li> <li>- manual lock (in microgravity it requires the help of an additional crewmember);</li> <li>- unintentional loosening over the time;</li> <li>- uncomfortable and bulky.</li> </ul>

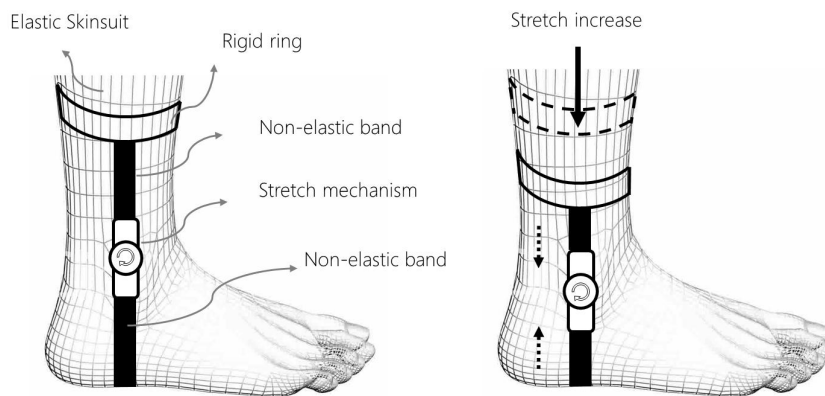


FIGURE 6.5: Load adjustment device - working principle

of the suit. Finally, it has to be light, compact, low-cost, able to withstand a maximum force around 150 N, and easy to use without the aid of another person.

### 6.3.2 Load Adjustment Mechanism

Several candidate mechanical devices were considered but, the *ratchet* mechanism, properly customized, was deemed to be the most suitable. A ratchet is a mechanical device that allows continuous linear or rotary motion in a single direction preventing reverse. A ratchet is one of the oldest of all mechanisms and its simplicity and reliability are the main advantages. It can bear a large load in relation to its size (Onwubolu, 2005). Basically, as shown in Figure 6.6, a ratchet mechanism consists of a ratchet wheel (1), a driving pawl (2), an arm (3), a locking pawl (4), and a support (0). The driving pawl engages the teeth of the ratchet wheel under the action of a spring, or its own weight. When the arm moves counter-clockwise, the driving pawl turns the ratchet wheel through a given angle. When the arm moves clockwise, the catch slips past one or more teeth, but the locking

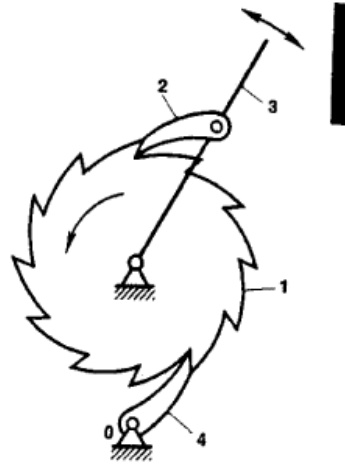


FIGURE 6.6: Ratchet mechanism - working principle

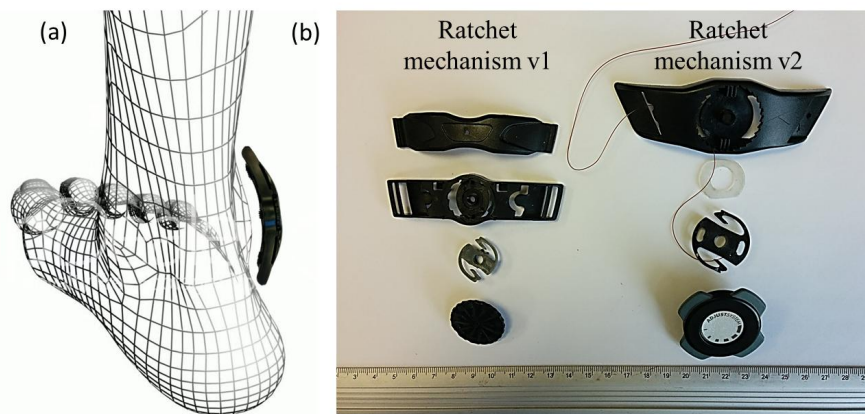


FIGURE 6.7: (a) Ratchet mechanism suitable shape with the malleolus and embeddable with SkinSuit. (b) Two different ratchet mechanisms with some mechanical improvement in order to enhance the robustness and usability.

pawl prevents the clockwise rotation of the ratchet wheel. Ratchets can be used to tension ropes or cables but are usually bulky and heavy.

However, the same principle can be re-adapted with a different geometry, in order to reduce the size and the weight whilst preserving efficiency. For instance, the ratchet adjustment mechanism used for bicycle helmets is light and compact used to adjust the internal size (Grim and Stroud, 2011). It was selected to adjust controllably the length of the SkinSuit's stirrups and fix it in a stable position. Figure (6.7) depicts the mechanism chosen and the relative placement on the body, enabling the compliance in terms of size and geometry with the ankles anatomy, compared to the original uncomfortable buckle clips.

### 6.3.3 GLCS Lower Body Simulator

After the requirements analysis and selection of the technology, the mechanism was re-adapted and tested in order to prove the feasibility of the implementation and the performance. Since each SkinSuit has to be individually tailored, a *GLCS simulator* was designed to test the adjustable mechanism. The current suit is able to produce a 20-25% of the g-force on the body at the maximum stretching level. Practically, after the donning, the SkinSuit has to be "activated" pulling up the stirrups to a fixed position. Over stretching across the suit is prevented by the inelastic *arrestor ribbons* aligned vertically along the suit, avoiding an over-extension of any specific 4 cm section of material. Thus, when the arrestor ribbons become completely flat to the suit, maximum stretch has been achieved. Furthermore, a preliminary test demonstrated that the SkinSuit, before the "activation", resulted already stretched at the torso, since the arrestor ribbons were completely flat. This led to the following considerations:

- without an "activation" from the bottom, the upper part of the suit produces a z-axis force, albeit minor, when it is put on;
- the z-axis force variation depends on the lower part of the suit, starting from the legs;

These remarks lead to consider the opportunity to focus the attention on the lower part of the suit, designing a "legs GLCS simulator", in which to embed the load adjustable mechanism and measure the relative effects. Considering a MK V SkinSuit and a subject whose body mass was 60 kg, the maximum z-axis weight force achieved by this suit is approximately 17 kg ( $F_{GLCS} = 167 N$ ), 25 % of the total weight. From this value, the small contribution of the torso has to be considered and subtracted from the total force produced. An experiment by using a half-body dummy dressed with the GLCS (Figure 6.8) the torso force contribution was defined by weights applied at the hips and then measuring maximum force required to stretch the arrestor ribbons. With a weight of 2.5 kg ( $F_{torso} = 24.5 N$  handlebar included), was required to completely the upper part of the SkinSuit wa. Therefore, the requirements needed for the lower body GLCS simulator experiment are:

- to mimic the elasticity of the suit;
- to produce a force around 140 N ( $F_{legs} = F_{GLCS} - F_{torso} = 164 N - 24 N = 140 N$ );
- to adjust the load of the simulator;
- to host the ratchet mechanisms;



FIGURE 6.8: GLCS torso load contribution

- to measure the force/load changes.

Figure 6.9(a) shows the initial version of the lower-body GLCS simulator in which the elastic cords simulate one leg of the suit and the frame allows to adjust the stretch. The elastic material and the soles are connected together with the adjustable ratched mechanism. The nominal length and the strength of the elastic cord were selected in order to achieve 70 N for each leg ( $140\text{ N}/2$ ). Stretch/force characterization was then performed in order to test the adjustable mechanisms under different load conditions. A cell load connected with the system measured the force change when the elastic cord was stretched with a  $\Delta\text{Length}$  ( $\Delta L$ ) of 50 mm until 500 mm. Characterization shown the expected liner relation between  $\Delta L$  and force (Figure 6.9 (b)), highlighting the maximum value reached by "one leg" of the suit equal to 73.5 N, proportional with the amount of Gz force that the GLCS is able to produce.

In order to performed a test as close as possible to the final application, Figure 6.10(a) and (b) depict the architecture and the final implementation of the entire GLCS lower-body simulator. The structure connected with a hospital bed allowed to change the length (hence the force) of the system varying the height of the bed with a dedicated lifting mechanism.

The first test was performed to prove the robustness of the ratchet mechanism, leading the force up to the maximum level and thus identifying the point of failure. Any mechanical failure was recorded during a cyclic stress test, in which the system was lead to the maximum stretch achievable and relaxed for 5 min continuously.

The second step was to demonstrate the effectiveness of the adjustable mechanism. Each ratchet mechanism was adapted to bear a force up to

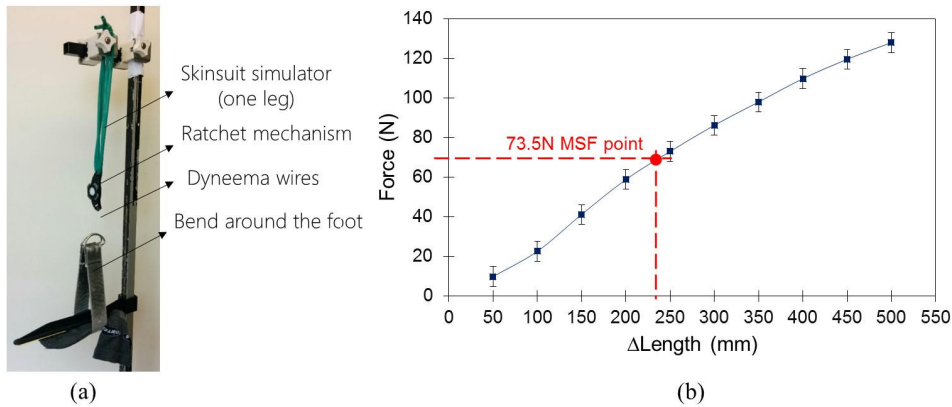


FIGURE 6.9: (a) Single-leg GLCS simulator. (b) Stretch-Load test of the lower body GLCS simulator with load cell (single leg) - Line to the best fit. MSF: Maximum SkinSuit Force

90 N before to reach the breaking point. A couple of mechanisms for each ankle were activated manually under a pre-loading condition of 50 N. The gear was turned for 4 times and the length variation was measured. Thanks to the previous length/force characterization, the graph in Figure 6.10 (b) shows the force variation generated by the ratchet mechanisms.

The results show some promising properties of the mechanism obtaining a  $\Delta L$  of 20 mm for each turn and thus a relative force variation  $\Delta Force$  equal to 20 N, therefore 5 N per turn. Then, the internal design of the mechanism with 80 teeth, allows to adapt the load with a sensitivity of 0.17 N.

In conclusion of this experiment a proof-of-concept of the load adjustable mechanism for the GLCS was presented, in particular the evaluation of the ratchet mechanism solution and its properties. The next step is related to the design and test a wearable Load Monitoring (LM) system integrated within the GLCS able to measure  $\Delta Force$  variation over the time.

## 6.4 Load Monitoring (LM) system - State of the Art

During the IRISS Space Mission performed by ESA astronaut Andreas Mogensen, one of the objective was to collect data about +Gz loading due to the SkinSuit. In terms of reliability tested during previous NASA experiments, the *Force-shoes* were candidate as measuring instrument to be used with the GLCS, in order to collect loads data of the Gz-load.

Designed by XSENS (*Xsens Force Shoes*), the Force-shoes (Figure 6.11) were used for the first time by NASA during exercise with the Advanced Resistive Exercise Device (ARED) on the International Space Station (ISS). The ARED uses adjustable resistance piston-driven vacuum cylinders along with a flywheel system to simulate free-weight exercises in normal gravity with

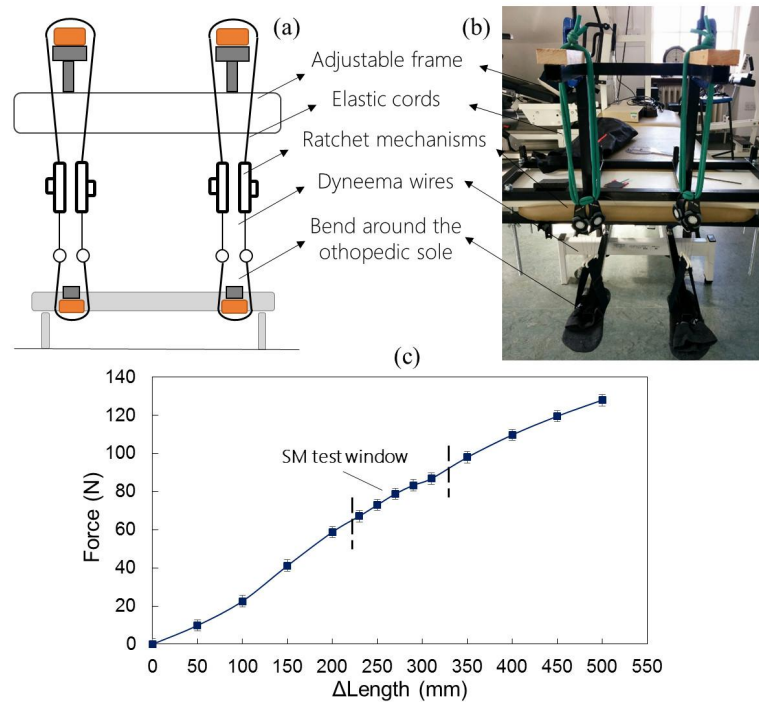


FIGURE 6.10: (a)Architecture of the full lower-body SkinSuit simulator. (b) Implementation of the simulator. (c) Characterization of the adjustable load mechanism.

the aim to retain strength, posture ability and functionality of the crew member's body (Fregly et al., 2013). The aim of the Force-shoes was to measure the exercise loads on the ARED with high accuracy, providing important data for current and future human research experiments in space (Hanson et al., 2014).

Although the reliability of the technology, the Force Shoes were not worn since the mission planners was shortened, skipping the Force Shoes tests. Furthermore, they are bulky, complex, does not provide a continuous real time Gz monitoring and take time to set up, a new simpler integrated load sensor system embedded within the SkinSuit, is the objective presented in the following section.

#### 6.4.1 Sensor Technology Selection

As mentioned previously, the SkinSuit Mark V is able to produce a vertical load along the body of around 20-25% of the body weight. In particular, the z-force vector is applied beneath the feet only on a portion of the stirrups that are rapped around the sole of the foot. The amount of the force is around 73.5N per foot applied on a surface of  $35\text{ cm}^2$ , measuring the stirrup area in contact with the foot. Therefore the resulting pressure is 21 kPa. The initial solution proposed was to instrument the stirrups with a flat and



FIGURE 6.11: Xsens Force Shoes

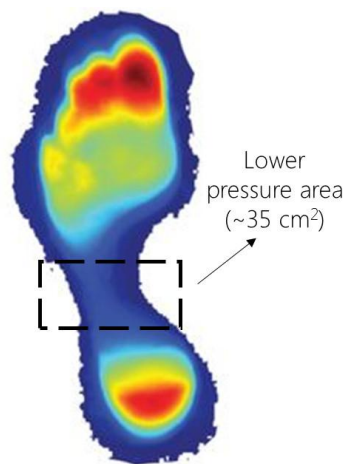


FIGURE 6.12: Sensor placement and standing weight distribution.

reliable force sensor. The selection of the suitable technology to be implemented takes into consideration the current plantar pressure technologies, normally used for podiatry, gait and posture analysis.

In taking any biomechanical measurements, devices must be optimized for the specific application to ensure that readings are accurate. Detailed analysis must be thoroughly undertaken prior to any measurements and for foot plantar system the sensor requirements have to be taken into consideration. The key specifications for the sensor performance include: linearity, hysteresis, pressure range, sensing area of the sensor, operative frequency, creep and repeatability, as detailed by Abdul Razak et al., 2012. In addition, the placement of the sensor is critical and, as explained in Par.6.12, the right placement was a trade-off between the sensor size and the sensing area.

There are a number of different commercial plantar pressure sensors including capacitive sensors, resistive sensors, piezoelectric sensors and piezoresistive sensors. These sensors provide electrical signal output (either voltage or current) that is proportional to the measured pressure. There

is a number of commercially available foot-pressure sensors but they generally do not fulfil the requirements of many biomechanical applications due to specifications (size of sensing area, user interface, fit comfort and portability) and performances limitations (pressure range and accuracy). A brief summary of the features of each technology, with the relative commercial products is listed below.

**CAPACITIVE SENSORS** - the sensor consists of two conductive electrically charged plates separated by a dielectric elastic layer. Once a pressure is applied the dielectric elastic layer bends, which shortens the distance between the two plates resulting in a voltage change proportional to the applied pressure.

Commercial products based on this system are the *emed*<sup>®</sup> platform systems (Novel, Germany) and *Pedar*<sup>®</sup> in-shoe systems (Novel, Germany) (*Novel Quality in Measurement*). Both not suitable for our application since the *emed*<sup>®</sup> is not embeddable with the SkinSuit and *Pedar*<sup>®</sup> has a bulky and hungry power electronic system.

**RESISTIVE SENSORS** - Force-Sensing Resistor (FSR) is a good example of resistive sensors. When pressure is applied the sensor measures the resistance of a conductive foam between two electrodes. The current flowing through the resistive sensor increases as the conductive layer changes (i.e., decreases resistance) under pressure. FSRs are made of a conductive polymer that changes resistance with force: the application of a force causes the conductive particles to touch increasing the current through the sensors (Shu et al., 2010). FSRs are flat and easily integrable with a fabric, make it suitable for our application.

Commercial products based on this principle are *MatScan*<sup>®</sup> platform systems and *F - Scan*<sup>®</sup> in-shoe systems (Tekscan, USA).

**PIEZOELECTRIC SENSORS** - produce an electric field (voltage) in response to pressure. The most suitable material for clinically oriented body pressure measurement is polyvinylidene fluoride (PVDF) because it is flexible, thin and deformable (Gefen, 2007). Piezoelectric devices have high impedance and therefore susceptible to excessive electrical interference that leads to an unacceptable signal-to-noise ratio.

Commercial products based on this system are Measurement Specialties, USA (*Measurement Specialties*) and PCB Piezotronics, Inc., USA (*PCB Piezotronics, Inc.*).

**PIEZORESISTIVE SENSORS** - are made of a semiconductor material. In Piezoresistive materials the bulk resistivity is influenced by the force or

TABLE 6.2: Comparison of in-shoe pressure sensors commercially available compared to Wahab et al., 2008.

	Wahab et al.	Textile Sensor	Parotec	Novel	Tekscan	Vista Medical
Sensor Size	2 mm	N.D.	2 mm	1.9 mm	0.15 mm	2 mm
Number of sensor	15	6	24	99	960	128
Pressure range(kPa)	3.000	800	625	1.200	1.034	260
Pressure sensitivity	N.D.	N.D.	N.D.	<7%	24%	N.D.

pressure applied: when the sensor is unloaded, the resistivity is high and when a force is applied the resistance decreases. When there is a pressure on the piezoelectric element (quartz crystal) the material produces electric charges from its surface. These charges create a voltage proportional to the applied force.

Commercial products based on this system are *FlexiForce*<sup>®</sup> (Tekscan, USA) and ParoTec (Paromed, Germany) (*Paromed*).

Sensors from Vista Medical, Novel and Tekscan show some performance limitations as they are made of sheets of polymer or elastomer leading to issues such as repeatability, hysteresis, creep and non-linearity of the sensor output (Table 6.2).

Considering the final application, in which the sensor has to bear peaks of pressure of about 20-25 kPa and has to be comfortable interfacing both with the flexible surface of the stirrup and the skin, the Force Sensing Resistor<sup>®</sup> (FSR) was selected, tested and characterized before being embedded into a GLCS.

Figure 6.13 shows the sensor the architecture of the system.

#### 6.4.2 FSR Characterization

Force Sensing Resistor (FSR) is a Polymer Thick Film (PTF) device which exhibits a decrease in resistance with an increase in the force applied onto the active surface. Its force sensitivity is optimized for use in human touch control of electronic devices. An overview of the FSR typical response behaviour is expressed via Force( $N$ ) vs Resistance ( $k\Omega$ ) characteristic plotted in Figure 6.14 (a), using data from the technical datasheet. The characterization was carried out with a stainless steel actuator with a 10.0 mm diameter hemispherical tip of 60 durometer polyurethane rubber. These data show a particular force-resistance characteristic being the response of evaluation

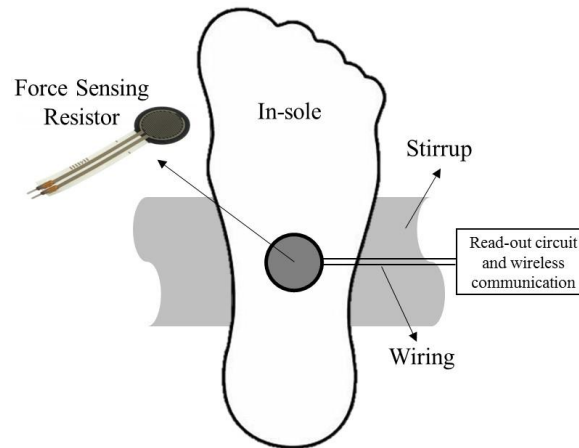


FIGURE 6.13: Load Monitoring system architecture.

part *FSR402* with 12.7 mm diameter circular active area. FSR resistance operates as more pressure is applied. When there is no pressure, the sensor looks like an infinite resistor (open circuit), as the pressure increases, the resistance goes down. At the low force end of the force-resistance characteristic, a switch like response is evident. This turn-on threshold, or "break force", that swings the resistance from greater than 100 k $\Omega$  to about 10 k $\Omega$  (the beginning of the dynamic range that follows a power-law) is determined by the substrate and overlay thickness and flexibility, size and shape of the actuator, and spacer-adhesive thickness (the gap between the facing conductive elements). Break force increases with increasing substrate and overlay rigidity, actuator size, and spacer-adhesive thickness. Eliminating the adhesive, or keeping it away from the area where the force is being applied, such as the center of a large FSR device, ensures it a lower rest resistance (e.g. stand-off resistance). The sensor reaches the saturation force beyond 10 kg. The saturation pressure of a typical FSR is in the order of 100 to 200 psi. Forces higher than the saturation force can be measured by spreading the force over a greater area; the overall pressure is then kept below the saturation point, and dynamic response is maintained. Figure 6.14 (c) depicts a Force-Resistance characterization according to the project requirements, in terms of force range and accuracy, showing a high measurement error with forces lower than 40 N and a small force variation between 40 to 100 N.

Figure 6.14 (b) shows the relation between the conductance ( $\frac{1}{R}$ ) and the force. This format allows interpretation on a linear scale. For reference, the corresponding resistance values are also included on the right vertical axis. It also includes a typical *part-to-part* repeatability envelope. The error band determines the maximum accuracy of any general force measurement. The spread or width of the band is strongly dependent on the repeatability of

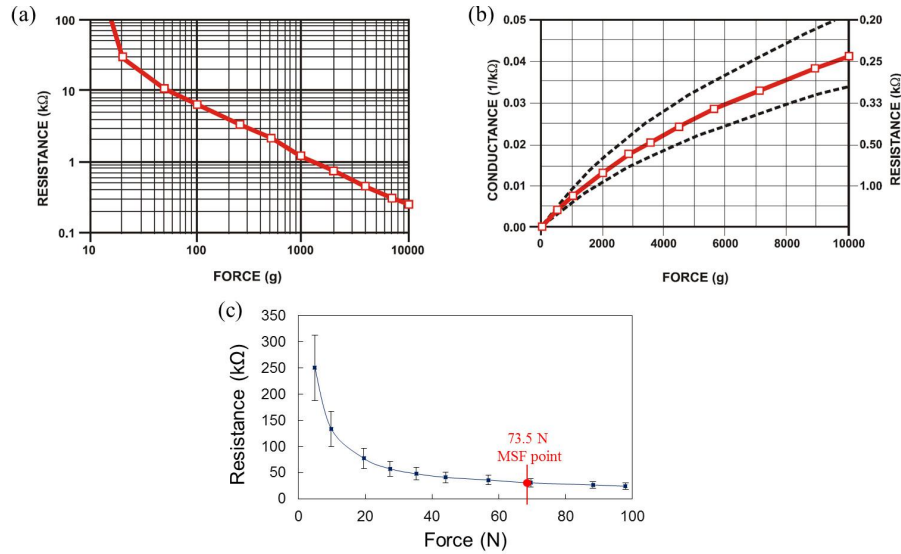


FIGURE 6.14: (a) FSR Force-Resistance characterization. (b) FSR Force-Conductance characterization. (c) Force-Resistance characterization simulated the GLCS conditions

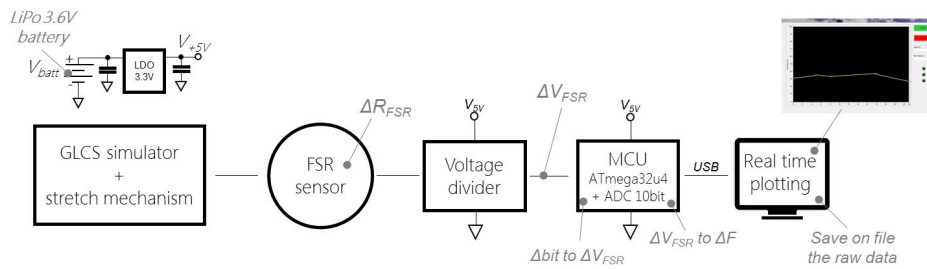


FIGURE 6.15: FSR System Architecture.

any actuating and measuring system, as well as the repeatability tolerance held by the manufacturer (Interlink Electronics) during FSR production. Typically, the *part-to-part* repeatability tolerance held during manufacturing ranges from  $\pm 15\%$  to  $\pm 25\%$  of an established nominal resistance.

### 6.4.3 FSR System Architecture

Figure 6.15 shows circuit used to test the sensors adopting a simple force-to-voltage conversion. The FSR device was tied to a measuring resistor in a voltage divider configuration ( $\Delta R_{FSR} \rightarrow \Delta V_{FSR}$ ). The sensor connected to the power supply with a +5 V Low-DropOut regulator (LDO) and to the pull-down resistor  $R_{fixed}$  to ground. The  $\Delta V_{FSR}$  of the voltage divider was connected to an ADC of a microcontroller. In accordance with the previous sensor characterization, the firmware code (see Appendix) flashed within the microcontroller was able to convert the  $\Delta V_{FSR}$  into a Force variation

( $\Delta F$ ). Finally, thanks to an ad-hoc user interface wrote in C#, the results were plotted in real time on a laptop.

The output of the voltage divider is described by the eq. 6.5

$$V_{OUT} = \frac{V_+}{\left(1 + \frac{R_{FSR}}{R_{fixed}}\right)} \quad (6.5)$$

In the shown configuration, the output voltage increases with the force applied. If  $R_{FSR}$  and  $R_{fixed}$  are swapped, the output swing will decrease with increasing force. These two output forms are mirror images about the line  $V_{OUT} = \frac{V_+}{2}$ .

The measuring resistor,  $R_{fixed} = 10k\Omega$ , was chosen to maximize the desired force sensitivity range and to limit current according to the datasheet (*Arduino Board Yun*). Following the datasheet, the current through the  $R_{FSR}$  should be limited to less than  $1 mA/cm^2$  with a force applied. A single sided supply LM358 op-amps was used to reduce the error due to the source impedance of the voltage divider. In this configuration the analog voltage reading from the microcontroller ranges from 0 V to about 5 V.

The source code(see Appendix) flashed onto the MCU (ATmega32u4) uses the embedded Analog Digital Converter (ADC) and allows an analog to digital conversion, following the eq. 6.6,

$$\frac{ADC_{resolution}}{Voltage\ supply} = \frac{ADC\ reading}{Analog\ voltage\ measured} \quad (6.6)$$

$$\frac{1023}{5\ V} = \frac{ADC\ reading}{Analog\ voltage\ measured} \quad (6.7)$$

In particular it is a 10-bit ADC, thus it is able to detect 1,024 discrete analog values. The MCU reads the analog value coming from the voltage divider ( $V_{FSR}$ ), converts to digital ones and calculates the resistance ( $R_{FSR}$ ) as described in eq. 6.8. By calculating the conductance ( $G_{FSR} = \frac{1}{R_{FSR}}$ ) the MCU is able to derive the Force ( $F_{FSR}$ ), in accordance with previous characterization expressed in Figure 6.14 (b).

$$R_{FSR} = \frac{(V_+ - V_{FSR}) \cdot R_{fixed}}{V_+} \quad (6.8)$$

The following tests were performed with the goal to evaluate the reliability of the system and repeatability of the measurements.

#### 6.4.4 Tests and Results

The FSR sensor was implemented and tested with the full lower-body GLCS simulator, in accordance with Par. 6.4.3 System Architecture. The experiment applied varying elastic forces with a  $\Delta L$  of in steps of 50 mm and

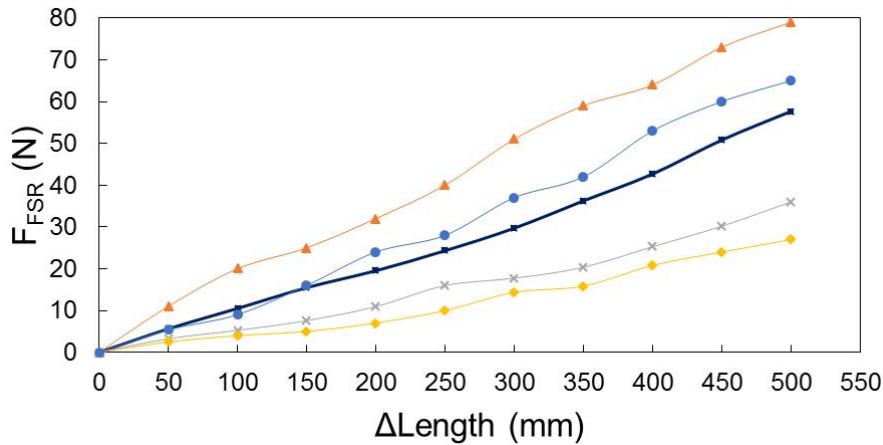


FIGURE 6.16: Reliability test of FSR with the lower body GLCS simulator.

reading the ( $F_{FSR}$ ) from the sensor system with an average of 50 samples for each measurement point.

Figure 6.16 plots the behaviour of the force sensor ( $F_{FSR}$ ) under different measuring set. The FSR sensor shows a linear behaviour at varying loads, however the repeatability is poor with standard deviation larger than 40%, with different measurements in the same experimental conditions. At a fixed  $\Delta L$  value corresponds different  $F_{FSR}$  values during different measuring sets, mainly due to the anatomy of the foot, to the flexibility of the stirrup and to slight movement of the sensor across the foot sole surface. The foot has not an uniform surface and anatomy with high and low pressure profile in different areas; besides the movable stirrup, therefore the relative position of the FSR sensor with the foot can not be fixed. Furthermore, higher values were recorded when the sensor moved accidentally near the edge of the foot, due to a cutting edge effect between the stirrup and the sole; while lower and variable values were recorded when the sensor moved in the middle of the sole.

Furthermore, with a force distributed on the top of the sensor, the values read by the system were different from the previous  $\Delta L$  vs *Force* analysis, because, as shown in Figure 6.17, the sensor has been designed to sense a pressure applied only within the "black rigid ring" portion. With a force applied over a larger area, the rigid ring absorbs part of the force, recording a lower force value from the sensor. To solve this issue, a squared FSR sensor was used, however the curved profile of the sole causes a deformation of the sensor and then a resistance variation without any load applied.

As only load monitoring system has to be reliable and the measurements repeatable without a re-calibration of the system over the time based on the results obtained with the FSR sensors, are not suitable for integration

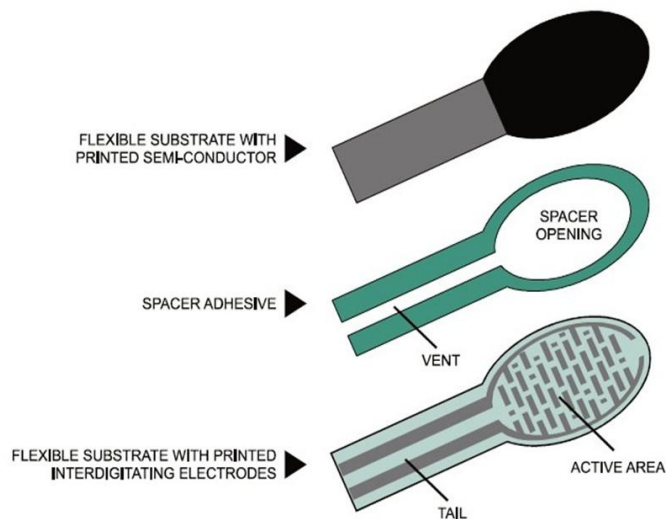


FIGURE 6.17: FSR structure.

with the GLCS.

To solve the issues reported and to respect the objectives of the project, in the next section a new technological approach is proposed.

## 6.5 Stretch Monitoring (SM) system

An alternative strategy is to measure the stretch of the suit. As described in 6.2.2, the GLCS gradually increases the tension in the vertical direction thanks to gradual distribution of the non-uniform stretch material. Exploiting the properties of the material, different stretch levels of the SkinSuit means different Gz-load values. Therefore measuring the displacement from two fixed points on the SkinSuit with a stretch sensor, allows to evaluate the amount of the stretch and thus the Gz-load applied by the suit. The solution proposed shown the following advantages:

- it is not affected by the foot anatomy;
- it is limited body-sensor interface;
- it can be easily customized for each GLCS.

Whereas, the challenges to overcome were:

1. to seek a suitable placement of the sensor on the SkinSuit followed by a previous suit stretch characterization;
2. to identify a wearable stretch sensor compliant with the elastic properties of the SkinSuit;

3. to characterize the sensor selected;
4. to integrate the stretch sensor coupled with a wireless read-out circuit within the SkinSuit;
5. to test and validate the system in the field.

### 6.5.1 GLCS stretch characterization

The structure of the GLCS Mark V, used for this evaluation, has a structure subdivided into 25 circumferential bands of about 3 cm of height and each band has arrestor ribbons aligned vertically to prevent over-extension of the material (see Figure 6.2). The stretch sensor, placed perpendicularly to the elastic bands, thus needs to be able to monitor local displacement. However, the vertical stretch is not uniform along the suit was worn and some portions are more stretchable than others. Therefore, it was necessary to characterize the GLCS in order to evaluate the amount of stretch in different areas and find the suitable placement for the sensor, in terms of range and variation of stretch.

Four different portions of the GLCS was characterized: torso, hips, upper leg and lower leg. Stretch characterization was performed by measuring the distance between the pairs of markers placed on each area with load. The nominal distance before stretch was to 60 mm, that is the height of two circumferential bands. Figure 6.18 (a) shows the experimental set-up. When the GLCS is completely stretched the highest load is reached. In order to determinate the load range the maximum load of the GLCS Mark V is around 20-25 % of the subject's body-weight and thus for this test the max load was up to 15-17 kg.

The delta elongation ( $\Delta L$ ) of each area at different loads is not linear, as shown in Figures 6.18 (b), highlighting that the GLCS was not designed for use with different loads but with a single design load. Thus, as expected each area behaves differently with the same load, however the torso is resulted completely un-stretchable after donning. Torso and lower leg portion show the major variation and in particular:

- no changes of the torso part is appreciated, resulting completely stretched since the beginning of the experiment without any loads;
- an approximate linear and constant stretch-load behaviour was observed in the lower leg area.

The results shown the lower leg portion as the best candidate for stretch sensor placement.

Finally, as introduced in Paragraph 6.2.2, the friction between the suit and the skin was another relevant aspect to be considered, given that it

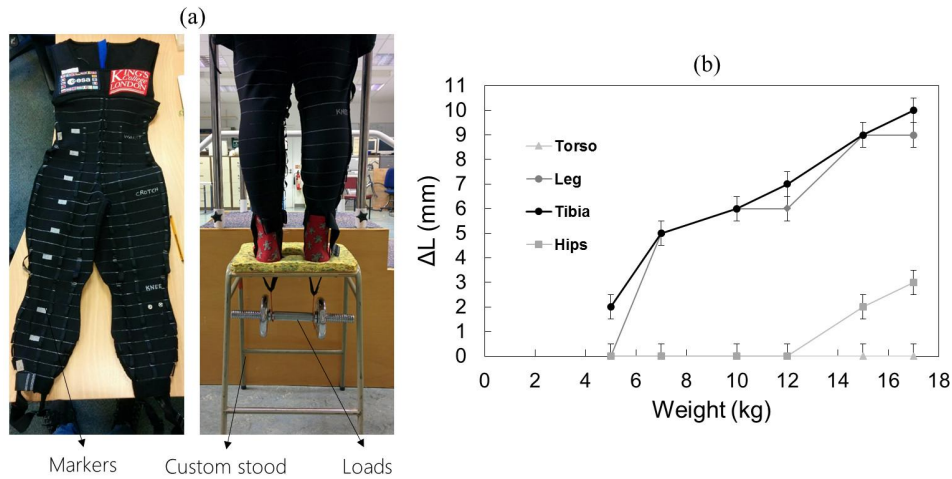


FIGURE 6.18: (a) Experimental set-up GLCS stretch characterization adjusting the Gz-load. (b) The four lines shows the stretching trend at different GLCS portion.

affects the stretch of the suit, compromising the linearity of the stretching. For this reason for the next part of the experiment, Talco powder has been used to reduce the friction.

### 6.5.2 Sensor - Material selection

The strain gauge is one of the most common technologies used to measure strain/stretch. A strain gauge provides an extremely simple and accurate way to measure even slight deformation of a solid surface or object. It is a relatively simple transducer that varies slightly in resistance when compressed or stretched, and can be bonded (using adhesive such as epoxy) to metal, plastic, wood, glass or other solids. Strain gauges made out of semiconductor material, like silicon or germanium, take advantage of the piezoresistive effect, a change in resistance that is greater than what can be explained by simple geometric deformation. Therefore strain gauges can reach high sensitivity  $< 1 \mu m$  and with a small active area of  $1-2 \text{ mm}^2$  (Hannah and Reed, 1992).

However, this type of the technology can not be used for wide displacement and to be embedded into a flexible substrate, such as a fabric. Nevertheless, exploiting the same principle of piezoresistivity, has been made a range of wearable piezoresistive sensors. They can be sub-divided mainly into three categories: conductive yarn, thick film and conductive fabric.

Usually the advantages of these sensor are the comfort and the easy integration into a fabric by conventional textile processing (Huang, Tang, and Shen, 2006; Melnykowycz et al., 2014; Gibbs and Asada, 2005). The drawbacks came out when read-out electronics, typically rigid and bulky, have

to interface with a fabric surface. It is very difficult to make a strong connection between the conductive yarns and electronics that need to be resistant to abrasion, wearing and washing. To address this issue, conductive polymers are widely used to develop conductive fabrics and in particular they are identified into two subclasses: intrinsically conductive polymers (ICPs) and conductive polymer composites (CPCs).

The ICPs can be coated onto the high elastic fabrics by an in situ chemical polymerization process (Brady et al., 2007; Scilingo et al., 2003). The result is a piezoresistive fabric with a strong variation of strain-resistance with time and a long response time. Paradiso et al., 2005 made a strain sensing fabrics by using CPCs. Composites made from carbon black filled silicone were coated onto high elastic fabrics showing a strain sensing properties between 5% and 35% of the strain.

Low complexity but high strain performing, stretch sensors can made be by conductive silicon (or conductive rubber) which could be integrated within the elastic fabric of the SkinSuit to measure the strain of the textile material under stretch. Conductive rubbers can be used as substitutes for traditional conductive materials, where lightweightness and flexibility are required: via the use of conductive fillers to achieve a low resistance the most common of which is black carbon .

A preliminary test was performed with the only available commercial product (conductive rubber cord *Conductive rubber cord*), depicted in Figure 6.19 (a). A 2 mm diameter rubber string impregnated with carbon-black with a nominal length of 40 mm was tested. Stretching the piezo-material with a step of 2 mm  $\Delta L$ , the resistance variation ( $\Delta R$ ) was measured with a bench digital multimeter. The results, depicted in Figure 6.19 (b), show a rapid resistance variation at the beginning of the elongation phase, reaching a plateau after only 4-6 mm of stretching. Then, only a slight changes was measured with further stretch. Furthermore, the material took several minutes (around 5 min) to revert to the original length and electrical resistance condition. The material was however able to be stretched up to the 70% of its nominal length.

The results demonstrate that this kind of sensor can not be used for the Stretch Monitoring system since:

- it has not a linear  $\Delta R$  variation at different elongation;
- it takes 5 mins minutes to revert to original condition (viscoelastic behaviour);
- it has a fast response following a stress but it tends to reach saturation after few 4-6 mm of elongation, which is less than the desired range of changes (around 20 mm);

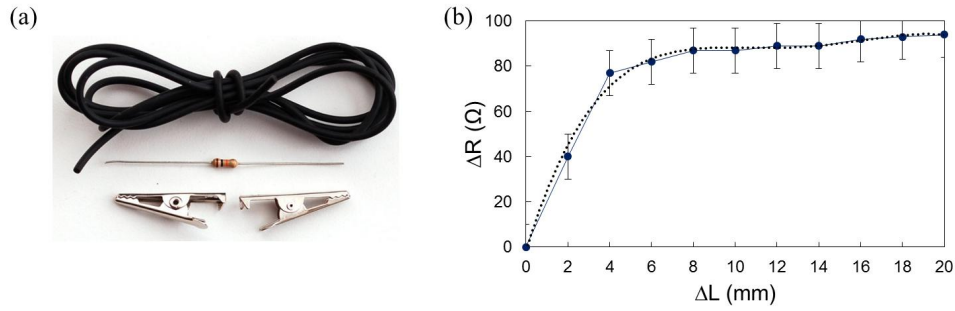


FIGURE 6.19: (a) Commercial stretch sensor. (b) Stretch-Resistance characterization.

TABLE 6.3: Conductive silicone ELASTOSIL 570/70 properties.

Typical characteristics	Inspection Method	Value
Hardness Shore A	DIN 53505	70
Crosslinker		C1 or C6
Appearance		black
Density	DIN 53479	$1.1 \text{ g/cm}^3$
Tensile strength	DIN 53504 S 1	$5.7 \text{ N/mm}^2$
Elongation at break	DIN 53504 S 1	140 %
Tear strength	ASTM D 624 B	$9.9 \text{ N/mm}$
Volume resistivity	DIN IEC 93	$2.8 \Omega/\text{cm}$
Compression set	DIN ISO 815-B	29 %

- its resistance changes after a bending of the material without stretch.

These critical aspects arise from the chemical composition of the conductive silicone and the moulded process. Therefore, to overcome the issues reported whilst maintaining the mechanical properties, the CLR with brand name ELASTOSIL 570/70 from Wacker Chemie AG (*Wacker ELASTOSIL*) has been chosen to develop a custom stretch sensor. It is an electrically conductive bi-component silicone rubber for press moulding and post curing. Table 6.3 summarizes the properties of the material.

In order to achieve the optimum electrical properties, it was post cured for 4 h at  $200^\circ\text{C}$  after moulding. The minimum crosslinking temperature is 170. The result was a layer of conductive silicone  $48 \text{ cm} \times 3 \text{ cm} \times 0.2 \text{ cm}$  (L x W x T) with resistivity of  $2.8 \Omega/\text{cm}$  (Figure 6.20).

### 6.5.3 Stretch Sensor - Characterization

The moulded layer of conductive silicone was cut to obtain different strips of material with different length, from 500 mm to 50 mm with a step of 50 mm, with a constant width and thickness, 3 mm and 2 mm respectively. The strips characterized by stretching the material with a step of 5 mm and measuring the resistance variation with a bench digital multimeter. The



FIGURE 6.20: Custom stretch sensor.

objectives of this experiment were to analyse the behaviour of the material under static mechanical stress and evaluate the presence of hysteresis during the relaxation phase (post-stretch release).

Figure 6.21 (a) collects the results each length sensors and the significant results can be summarized as follow:

1. the linear resistance variation under static mechanical stress, independently from the nominal length;
2. the low hysteresis during the relaxing phase, with the stretch and relaxation lines almost overlapped and a relaxation time around 2-3 sec;
3. a short latency to return to the nominal length during the unload phase;
4. in average, the total elongation was  $\sim 70\%$  of the nominal length.

In comparison with the commercial conductive rubber cord, the custom material has an electrical behaviour suitable with the project requirements, ensuring a fine measurement of the GLCS stretch, and thus vertical load changes. Moreover, no observable electrical changes were recorded during the bending of the material. In order to address the issue of the short latency to return to the initial length, during implementation a sensor pre-stretched of the  $\sim 10\%$  of the nominal length is required.

#### 6.5.4 Stretch Sensor - System Architecture

The polymeric transducer changes its physical and electrical properties in response to an external stimulus and this changes needs to be converted into an electrical signal through a dedicated Read-Out Circuit (ROC). The resistance variation is a continuous physical quantity that has to be interfaced with a digital system. Generally, a voltage divider coupled with an

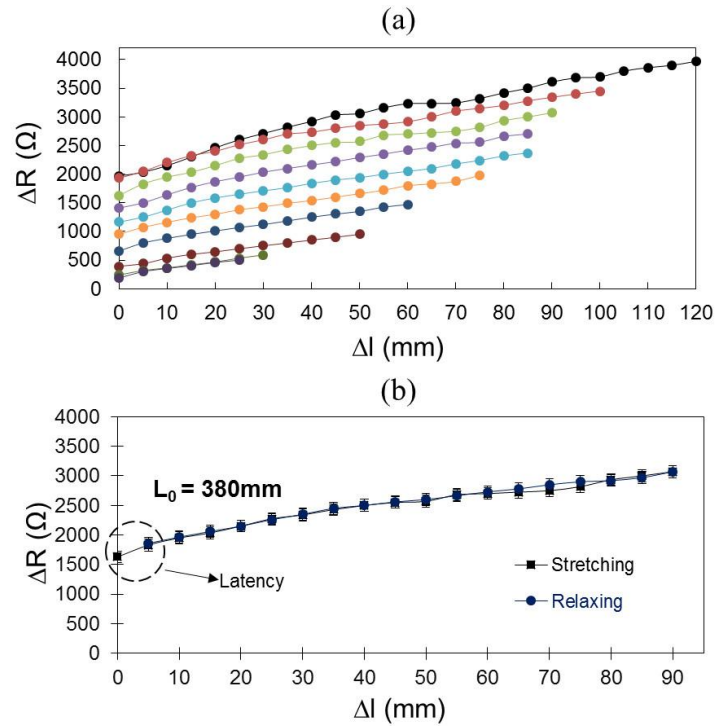


FIGURE 6.21: (a) Stretch sensor characterization at different nominal length. (b) Stretching-Relaxing test

Analog to Digital Converter (ADC), converts a voltage quantity into a digital number. The conversion involves quantization of the input, so it necessarily introduces a small degree of error. Furthermore, instead of continuously performing the conversion, an ADC does the conversion periodically, sampling the input. The result is a sequence of digital values that are converted from a continuous-time and continuous-amplitude analog signal to a discrete-time and discrete-amplitude digital signal. With the proper mixed analog-digital approach it is possible to encode the analog information in the time-domain with a robust and reliable periodic digital signal. The quasi-digital approach is able to preserve the original information with high accuracy. The ROC, designed using a Schmitt Trigger oscillator, allows converting of an analog signal into a quasi-digital signal. The output is a square wave able to change its frequency according to the resistance value of the transducer.

Figure 6.22 depicts the SM system architecture comprised of the stretch sensor ( $\Delta R_{sens}$ ), the analog-to-quasi digital ROC ( $\Delta f$  output), the microcontroller, the Bluetooth module and the custom graphic user interface. The overall system was powered with a 3.7 V 200 mAh LiPo rechargeable battery coupled with a fixed 3.3 V voltage regulator.

The sensor was embedded within the GLCS with conductive thread providing the interface and the electrical connection with the ROC. Figure 6.23

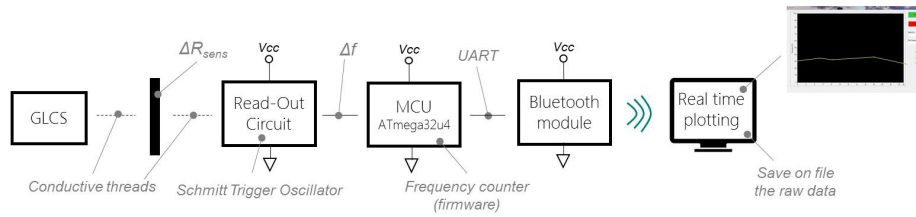


FIGURE 6.22: Stretch Monitoring system architecture.

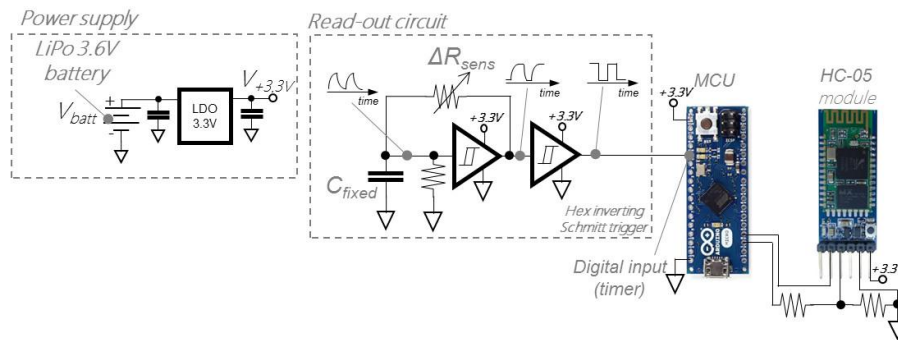


FIGURE 6.23: Circuit schematic of the SM system.

shows the circuit schematic of the system. The ROC is based on a Schmitt Trigger Oscillator in which the transducer is used as feedback element of the circuit. Schmitt trigger is a bistable multivibrator used as relaxation oscillator. This is achieved by connecting a single  $R_{sens}C_{fixed}$  series between the output and the input of an inverting Schmitt trigger. The output will be a continuous square wave whose frequency depends on the values of  $R_{sens}$  and  $C_{fixed}$ , and the threshold points of the Schmitt trigger. Here, a comparator-based Schmitt trigger is used in its inverting configuration.

The HEF40106B hex inverter was used, which provides six CMOS inverting buffer with high noise immunity, high bandwidth, high gain and excellent input/output characteristics producing a more “squared” output waveform compared with standard TTL logic gates. The inverting buffer switches at different points for positive-going and negative-going signals. The difference between the positive voltage ( $V_{T+}$ ) and the negative voltage ( $V_{T-}$ ) is defined as hysteresis voltage ( $V_H$ ). The digital Schmitt trigger gate has a built-in hysteresis  $V_H$  (0.8 V) and the threshold voltages are ( $V_{T+}$ ) (1.6 V) and  $V_{T-}$  (0.8 V).  $R_{sens}$  connects the circuit in a positive feedback loop necessary for oscillation. Figure 6.24 (a), (b) and (c) show the electrical characteristics of the HEF40106B with  $V_{DD} = 3.3 V$  and  $V_{SS} = 0 V$ . The output changes with a propagation delay equal to 75 ns when the input voltage rises above 66% and falls below 33%. The capacitor in a Schmitt Trigger

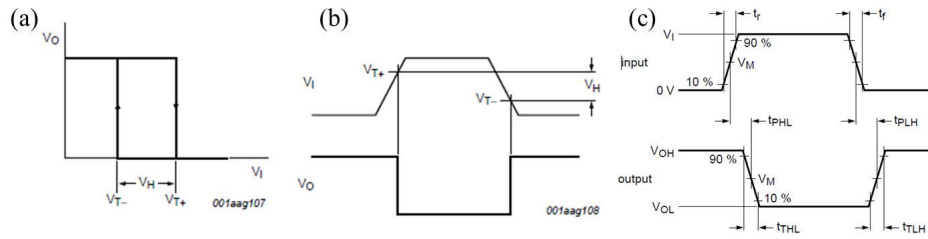


FIGURE 6.24: HEF40106B (a) transfer characteristics, (b)  $V_{T-}$ ,  $V_{T+}$  and  $V_H$  waveforms definition and (c) delay propagation and output transition time.

Oscillator must charge to 66 % of rail voltage to make the output go LOW, then discharge to 33 % of rail voltage to make the output goes HIGH. The capacitor takes time to charge or discharge between these two values and this gives the oscillator a known frequency of operation. In addition to the first Schmitt Trigger output, a second inverter was used to square perfectly the output, with a inversion of the phase. Following the configuration proposed, the delay time variation (or frequency shift) is determined by the values of  $R_{sens}$ .

- when  $V_C$  is less than  $V_{T-}$ ,  $V_O$  goes high (3.3 V) and starts charging the capacitor  $C$  through  $R_{sens}$ ;
- when  $V_C$  crosses the threshold voltage  $V_{T+}$ ,  $V_O$  goes low (0.05 V) and the discharging of  $C$  through  $R_{sens}$  begins;
- when  $V_C$  crosses the threshold voltage  $V_{T-}$ , the initial step is repeated, generating an output oscillation.

The output frequency is given by the following Eq. 6.9

$$f = \frac{1}{t} = \frac{1}{t_h + t_l} \quad (6.9)$$

where the period  $t$  is the sum of the period when output is high  $t_h$  and when it is low  $t_l$ . To derive the frequency equation and in particular  $t_h$  and  $t_l$  the universal time constant formula (Eq. 6.10) for the  $RC$  circuit was used with the following parameters  $V_{T+} = 2V$ ,  $V_{OH} = 3V$ ,  $V_{T-} = 1.5V$ ,  $V_{OL} = 0.05V$  and  $V_H = 0.5V$ .

$$change = (final - start)(1 - e^{-\frac{t}{RC}}) \quad (6.10)$$

$$V_c(t) = V_f - (V_f - V_i)e^{-\frac{t}{RC}} \quad (6.11)$$

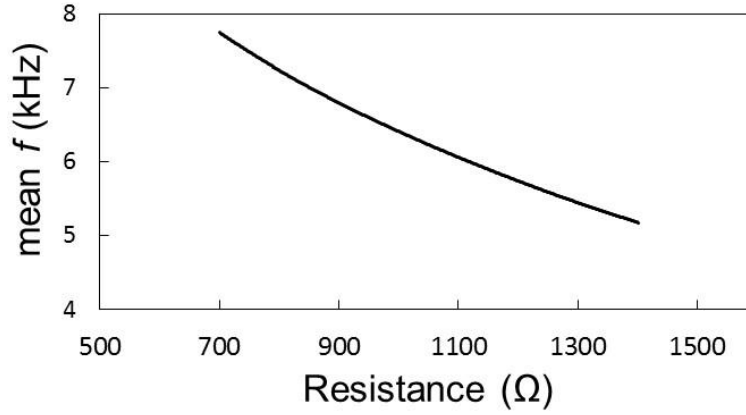


FIGURE 6.25: Schmitt Trigger simulation.

where  $V_c(t)$  is the capacitor voltage change,  $V_f$  is the capacitor voltage at infinity and  $V_i$  is the initial voltage of the capacitor. The Eq. 6.10 can be written for  $t_h$  and  $t_l$ , as follow:

$$V_H = (V_{OH} - V_{T-})(1 - e^{-\frac{t_h}{RC}}) \quad (6.12)$$

$$V_H = (V_{OL} - V_{T+})(1 - e^{-\frac{t_l}{RC}}) \quad (6.13)$$

and respectively,  $t_h = 0.26R_{sens}C$  and  $t_l = 1.62R_{sens}C$ . Considering the Eq. 6.9, the output frequency is

$$f = \frac{1}{t_H + t_L} = \frac{0.62}{R_{sens}C} \quad (6.14)$$

Figure 6.25 shows the LTspice simulation of the circuit with a frequency sweep from 700 Ω to 1400 Ω and step frequency of 1Hz.

### 6.5.5 Results and Discussion

The experiment performed using the set-up shown in Figure 6.26 (a). The Stretch Monitoring (SM) system with read-out circuit, MCU, Bluetooth Module and LiPo battery was assembled and integrated within a small "black box" with size of 65×27×27 mm (L×H×W) in order to be portable and attachable on one leg of the GLCS. The stretch sensor was embedded within the textile structure of the SkinSuit and connected with the SM system through conductive threads sewn within the elastic fabric. Two metallic snap-fasteners stitched with conductive threads provide a robust and comfortable electrical connection the SM system. A second stretch sensor has been embedded on the other leg of the SkinSuit and connected with a digital multimeter in order to compare simultaneously the  $\Delta R$  and  $\Delta f$  variation during the experiment. The objective of the experiment was to prove the

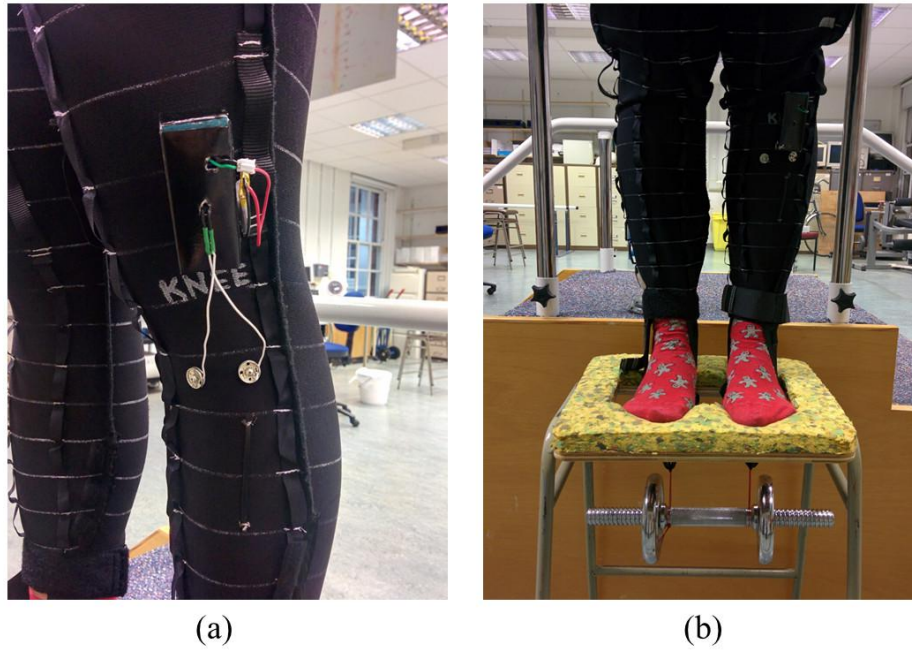


FIGURE 6.26: (a) Stretch Monitoring system implementation on the GLCS. (b) Experimental set-up adjusting the Gz-load of the suit.

SM system effectiveness with different loads level. As shown in 6.26 (b), the subject with the SkinSuit was standing on a custom stool and different weights (0-17 kg of range) were hung on beneath to simulate different Gz-force. Through the custom user interface it was possible to monitor the real time load change through the SkinSuit.

Figure 6.27 depicts the results of the  $\Delta R$  and  $\Delta f$  in relation with the force and length variations of the SkinSuit. Thanks to the previous characterizations, it was possible to determinate the amount of Gz force produced in relation with the length-force variation. The behaviour of the stretch sensor was almost linear for each leg. However, the friction between the skin and the suit had to be considered. Indeed, an increase of the stretch of the suit was obtained with a movement of the subject using a fixed weight. This aspect was measured by the sensor with a rapid variation of  $\Delta R$ , and therefore  $\Delta f$  with a constant load. The system, powered with a 3.6 V 250 mAh LiPo battery provided a life time of 3 h with a continuous stream a rate of 10 Hz, adjustable from the user interface to save battery life or improving the data capture.

Thus, the SM system provides a real-time and potentially reliable monitoring of the Gz variation by the GLCS. Furthermore the system can be easily installed and removed from the SkinSuit if required during donning and doffing. A further integration of the electronics would enhance the efficiency of the system in terms of power consumption and overall size.

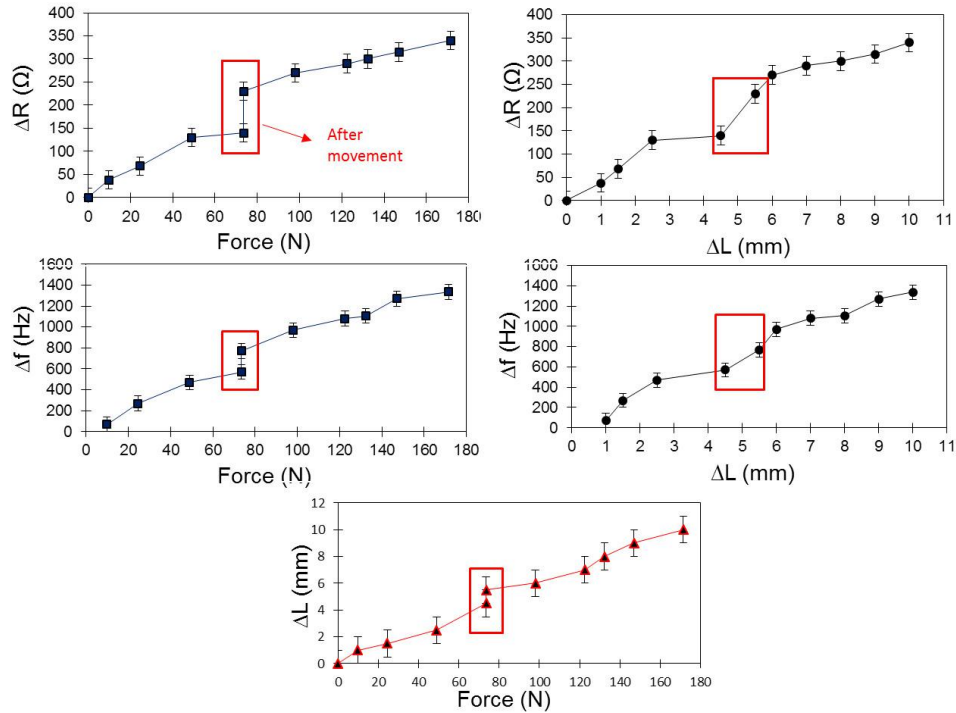


FIGURE 6.27: Stretch Monitoring system tests ( $F - \Delta R$ ), ( $F - \Delta f$ ), ( $\Delta L - \Delta R$ ), ( $\Delta L - \Delta f$ ) and ( $F - \Delta L$ ).

## 6.6 Spinal Elongation Monitoring System

Gravity affects the musculoskeletal system and in particular the spine. During sleep (4-8 h) the body can elongate 1.3-2 cm thought to be due to loss of a hydrostatic pressure gradient inducing intervertebral disc expansion. In space this process is increased resulting in up to 6.9 cm stature elongation. Currently, the spine elongation is monitored adopting standard measurement tools, such as stadiometer or tape measure. On board the ISS this analysis is usually assessed by repetitive measurements of the height, marked on the internal wall of the space module taking note of the elongation over time (Figure 6.28).

In this Chapter, a wearable, non invasive and integrated Spinal Elongation Monitoring (SEM) device is presented for potentially use in space. The system consists of a stretchable sensing material coupled with a custom electronic circuit directly attached on the body and, in particular, on the portion of the spine that has to be monitored. The round PCB circuit, with a surface area measured by  $\sim 15 \text{ cm}^2$ , provides a read-out circuit, able to convert the length variation of the sensor into a quasi-digital signal characterized by a frequency sensitivity, on average of  $80 \text{ Hz/mm}$ , and a low energy wireless communication based on Bluetooth Low Energy (BLE) or IR-UWB selectable with a physical switch, in order to allow a direct compare



FIGURE 6.28: Height measurements on board the ISS.

of efficiency and power consumption of the two transmission technologies. Two standard 55 mm ECG electrode (*Convidein ECG electrode*) were used to mount the sensors allowing a stable contact with the skin of the subject with low risk of irritation.

The main objective of the SEM system is to monitor autonomously spinal elongation involved by a novel 0-g simulator called Hyper-Buoyancy Flotation (HBF), designed by King's College London. With 5 h of experiment session, the spinal elongation was monitored in selective portions of the spine with an accuracy of 1 mm. The data are transmitted to the user interface in real-time mode, ensuring a direct and fine control of the elongation status. Two stretch sensors, connected to a multimeter and coupled with the SEM system, were used to record the elongation in thorax region (T2-T4 vertebrae) and lumbar region (T12-L2 vertebrae) of the spine, measuring respectively an average length variation of 3 mm and 5 mm during the experiment. .

### 6.6.1 Background

The exposure to microgravity induces significant deconditioning of the musculoskeletal and cardiovascular systems, that may compromise health and functionality in space (Convertino, 2009). Spinal elongation is just one of the factors that can also affect the safety and performance of a crewmember while in space. Spinal elongation occurs due to the lack of gravity/-compression on the spinal column. This may also induce flattening of the natural spinal curvatures. Lumbar back pain, also known as Space Adaptation Back Pain is a common symptom experienced by astronauts during early exposure to spaceflight (Thornton, Hoffler, and Rummel, 1977; Styf,

Kalebo, and Hargens, 1994; Kerstman et al., 2012). Such pain has the potential to interrupt challenging in-flight tasks by reduction of restorative sleep and mental concentration. To date, there is lack of quantitative research addressing spinal adaptations and origins of lumbar back pain before, during and after spaceflight. The Flight Medical Clinical NASA Johnson Space Center concluded that among Shuttle orbiter crew members, the 68% report some degree of low back pain during spaceflight (Wing et al., 1991).

Therefore, to ensure an exploration class mission preserving astronaut's health, wellbeing and performance, effective countermeasures are urgently required (Young, 1999). During Apollo-Soyuz Test Project (ASTP) and Skylab, spinal elongation data was collected from a small number of subjects in a standing posture indicating a rapid increase in stature during the first few days of weightlessness, after which stature reached a plateau up to an increase of the 3% (Annis, 1978; Young and Rajulu, 2011; Bungo et al., 1987).

Whilst, devices such as Advanced Resistive Exercise Device (ARED), vibration isolated treadmill (T2) and Cycle Ergometer with a Vibration Isolation and Stabilisation System (CEVIS) are used for 2.5 hours of physical exercise to counteract the effects of the 0-g environment on the human body until recently back pain was neglected. More recently, 52% of the astronauts (Sayson et al., 2013), presumably secondary to the increased risk of disc injury (Johnston et al., 2010), a degeneration of spinal stabiliser muscles (Debusse et al., 2013) and stature elongation partly induced by saturated intervertebral discs and changes in spinal curvature (Sayson et al., 2013).

To acutely reduce back pain, the astronauts tend to adopt an embryonic flexion position. Height measurement is performed on the ISS with standard anthropometric tools, by marking the height on the internal wall of a space module (Figure 6.28). Several data were collected during last decades, especially with Skylab (Johnston and Dietlein, 1977), however selective spinal measurements have never performed, due to a practical challenges. On Earth, the height changes of intervertebral discs can be performed only with radiologic assessments (MRI or CT) but with the clear issue to simulate the weightlessness condition.

Vertebral column has 24 intervertebral discs interposed between the vertebral bodies: six in the cervical, twelve in the thoracic and five in the lumbar region, with one between the sacrum and coccyx (Figure 6.29). The discs account for approximately one-quarter of the total length of the vertebral column, and are primarily responsible for the presence of the various curvatures. On descending the vertebral column, the discs increase in thickness, being thinnest in the upper cervical region and thickest in the lower lumbar. In the upper thoracic region, however, the discs appear to narrow slightly. In the cervical region the disc is about two-fifths the height of the vertebrae, being approximately 5 mm thick. In the thoracic region the discs

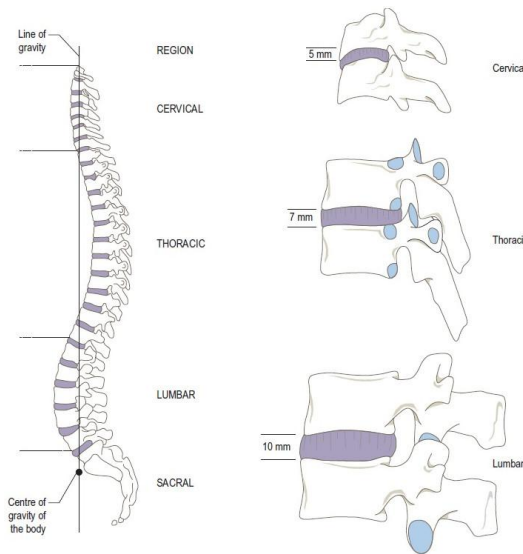


FIGURE 6.29: Vertebral column anatomy.

average 7 mm in thickness, so that they are one-quarter of the height of the vertebral bodies. The discs in the lumbar regions are at least 10 mm thick, equivalent to one-third of the height of the lumbar vertebral bodies. The relative height of the disc to the vertebral bodies is an important factor in determining the mobility of the vertebral column in each of the regions. Individual discs are not of uniform thickness; they are slightly wedge-shaped in conformity with the curvature of the vertebral column in the region of the disc. The curvatures in the cervical and lumbar regions are primarily due to the greater anterior thickness of the discs in these regions (Liem et al., 2001).

### 6.6.2 System Architecture

The Spinal Elongation Monitoring (SEM) system comprises of a piezo-resistive stretch sensor, a read-out circuit, a wireless low power data transmission and a re-chargeable battery. Figure 6.30 shows the System Architecture able to select the wireless communication technology to use, between Bluetooth Low Energy (BLE) and Impulse Radio-UltraWide Band (IR-UWB). This approach allows data to be transmitted for a short-range with a low power consumption, coupled with a compact design of the system. Furthermore, a double communication system allows is to be suitable with the Bluetooth receivers used by European Space Agency on the ISS and, thanks the IR-UWB technology, to provide a lower power consumption in compare with BLE for the next generation of wearable device. The overall system has to be placed directly on the back in a precise portion of the spine to be investigated.

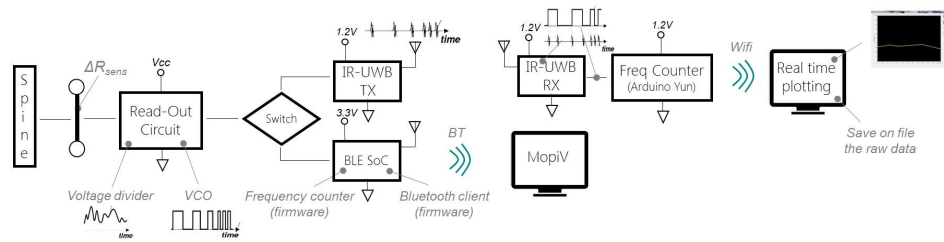


FIGURE 6.30: Spinal Elongation Monitoring (SEM) system architecture.

The elongation of the selected region of the spine is recorded by the stretch sensor that is able to change its electrical resistance ( $\Delta R$ ) proportionally to its axial deformation. The sensing material was chosen in order to be compliant as much as possible with the stiffness of the skin. The  $\Delta R$  produced under spine elongation is converted with a voltage divider into a voltage variation ( $\Delta V$ ), becoming the input of the Voltage Controlled Oscillator (VCO). The VCO generates an output oscillation frequency by the voltage input and in particular a frequency modulation due to the  $\Delta V$  input. The result is a quasi-digital signal (as explained in Chapter 2) able to encode the analog information into a digital frequency variation ensuring a reliable and high noise immunity signal output. Then, selecting the IR-UWB communication, as presented in Chapter 3, the VCO output is able to digitally trigger the generation of low energy pulses (30 pJ energy per transmitted pulse) from the IR-UWB transmitter with a 3.5 GHz of center frequency and bandwidth ranging of 300 MHz-500 MHz. The information transmitted needs a IR-UWB receiver able to regenerate the modulated signal and, with an external Micro-Controller Unit (MCU) to process the data.

Conversely, a SoC BLE-MCU provides a fully integrated solution with a pre-processing of the VCO signal, recording the frequency shift, and with a previous pairing process, a packet-based Bluetooth communication with other Bluetooth devices, used as receiver. Despite this integrated solution, this advantage is mitigated from the higher power consumption than IR-UWB, as presented in Chapter 3. Finally, the results of the experiment are plotted in real time on a custom user interface wrote in C#, which is also able to save the raw data of the length variation of the sensor.

### 6.6.3 Material Characterization

According to the experiment objectives, two different regions of the spine (thorax and lumbar) were monitored during a flotation experiment. The nominal length of the sensors have to be consistent with the anatomy of the spine involving selectively of 3-4 vertebrae, through anthropometric data

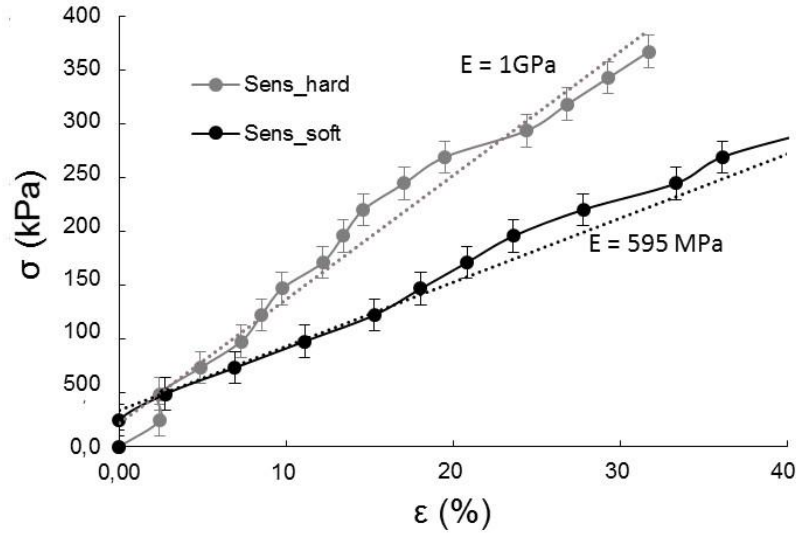


FIGURE 6.31: Spinal Monitoring sensor characterization of the stretch sensor v1 (hard) and v2 (soft) – Stress–strain curve.

(Cramer and Darby, 2013). The nominal length selected were 40 mm and 60 mm for the thorax portion (T2-T4 vertebrae) and the lumbar portion (T12-L2 vertebrae), respectively.

The first approach was to develop the sensor using the same piezo-resistive material used for the "Stretch monitoring system". However the stiffness of the material was greater than mechanical compared with mechanical properties of the skin. As human skin shows a heterogeneous, anisotropic, viscoelastic and non-linear stress-strain relationship (Agache et al., 1980), thus a stretch sensor with a low elastic module ( $E$ ) around 100–500 MPa is needed to prevent an elastic return phenomena of the material when it is placed on the skin. The conductive silicon material, based on Wacker Elastosil<sup>®</sup> R 570/50, was selected to improve the mechanical properties of the sensor maintaining a linear electrical resistance variation under strain. Experimental set-up in which calibrated weights, a calipers and a digital multimeter was used to characterize two thin stripes of piezo-material with a nominal length of 40–60 mm and a section area of  $4 \text{ mm}^2$ . To reduce the stiffness of the sensor, as close as possible with average skin stiffness, the Young Modulus of the sensing material was measured. Figure 6.31 shows the stress-strain curve of both materials highlighting a lower Young's modulus ( $E$ ) of the new material in comparison with the previous sensor. The Young's modulus is a measure of the stiffness of the material and it is defined as the relationship between the tensile stress ( $\sigma$ ) and strain ( $\varepsilon$ ) in the elastic field, as shown by the Eq. 6.15,

$$E = \frac{\sigma}{\varepsilon} = \frac{\frac{F}{A_0}}{\frac{\Delta L}{L_0}} \quad (6.15)$$

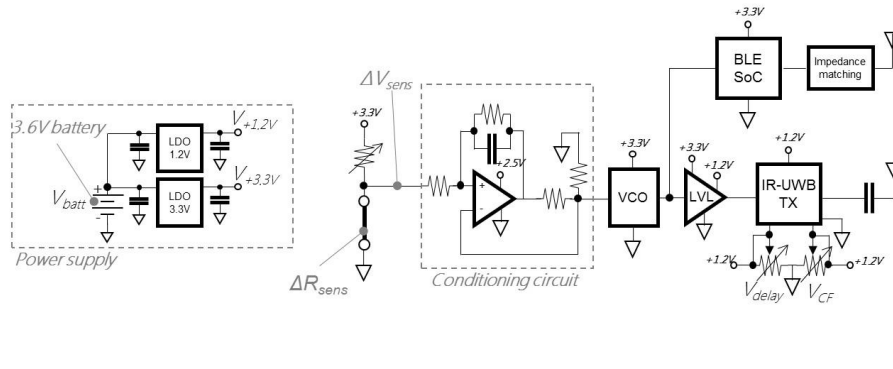


FIGURE 6.32: Block scheme of the SEM system.

where  $F$  is the force exerted on the material under tension,  $A_0$  is the actual cross-sectional area through which the force is applied,  $\Delta L$  is the amount by which the length of the material changes and  $L_0$  is the original length.

Furthermore, the elastic deformation limit was improved reaching the 62% of the nominal length in compared with the previous 31%. Finally, as shown by Figure 6.31 a piezo-electric characterization for both 40 and 60 mm sensors was performed with different calibrated weight. Resistance sensitivity under stress of  $61 \Omega mm$  and  $82 \Omega mm$  for 40 and 60 mm length sensors, respectively, was measured. These results allow to calculate the amount of resistance shift during the stretch phase, required to determinate the spinal elongation.

#### 6.6.4 Demonstrator and Implementation

##### A. Hardware Design

Figure 6.32 shows the block scheme of the SEM system. In order to optimize the PCB size, SMD components with a 0402 package for passive components and a QFN, SOT23 and TSSOP package for active components was selected. The system is supplied with a 3.6 V LiPo rechargeable battery with 150 mAh capacity connected with a standard 2-pin JST-PH connector to the PCB board. Then, two linear voltage regulators (Low DropOut regulator—TPS71712/33) with a fixed voltage of 1.2 V and 3.3 V supplies respectively the IR-UWB IC transmitter and the read-out circuit plus BLE—MCU SoC. The  $\Delta R_{sens}$  applied to the voltage divider generates a  $\Delta V_{sens}$  that was adapted to the input range of the VCO through the 20 k $\Omega$  trimmer  $R_T$ . The VCO is a LTC6990 voltage controlled silicon oscillator capable of operating in 488 Hz–2 MHz frequency range and providing <1% frequency drift across 0–100 °C, thanks to the dedicated conditioning circuit, as widely explained in Chapter 3.

A SMD slide switch allows selecting the IR—UWB or BLE wireless technology. With the IR—UWB, the output of the VCO which has an amplitude

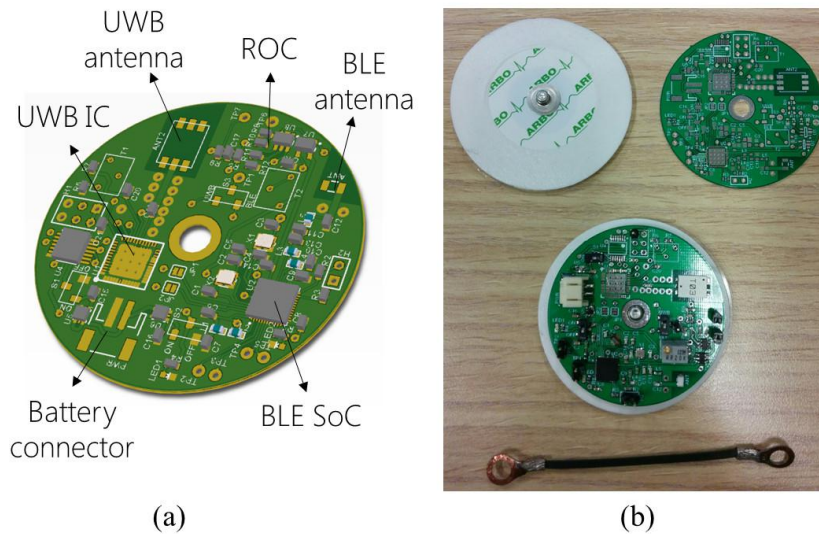


FIGURE 6.33: (a) SEM system altium design. (b) SEM system PCB and assembly

of 3.3 V has to be adapted since the UWB chipset works at 1.2 V. A bidirectional logic level translator (ADG3304) with  $V_{CCY} = 3.3\text{ V}$  and  $V_{CCA} = 1.2\text{ V}$  used to shift the voltage level of the oscillating signal from 3.3 V to 1.2 V. The UWB IC presented in Chapter 3, implements a flexible UWB pulse generator triggered by the VCO signal. The chip antenna (Tayo Yuden) filters the UWB signal in the 3.1–10.6 GHz band. The system provided two analog controls  $V_{DELAY}$  and  $V_{CF}$  to set the pulse duration and the center frequency  $f_c$ . The integrated transmitter consumes a measured 30 pJ energy per transmitted pulse.

Conversely, selecting the BLE communication system, the VCO signal flows directly to the GPIO pin of the commercial Bluetooth SoC (Nordic nRF51822). It is a flexible multiprotocol SoC ideally suited for Bluetooth Low Energy wireless applications. The nRF51822 is an ultra-low power 2.4 GHz wireless SoC integrating a 2.4 GHz transceiver, a 32 bit ARM<sup>®</sup> Cortex<sup>™</sup>-M0 CPU, a flash memory, and 31-pins analog/digital peripherals. A well designed PCB is necessary to achieve good RF performance, in particular the RF matching network, since a poor layout can lead to loss in performance or functionality. Especially in the case of the antenna matching circuitry (components between device pins ANT1, ANT2, VDD-PA and the antenna), any changes to the layout can alter the behaviour of the SoC, leading a degradation of the RF performance.

All the reference circuits are designed for use with a  $50\ \Omega$  single end antenna. A matching network is needed between the differential RF pins

ANT1 and ANT2 and the antenna, to match the antenna impedance (normally  $50\ \Omega$ ) to the optimum RF load impedance for the chip. The DC supply voltage has been decoupled as close as possible to the VDD pins with high performance RF capacitors. Following the *Antenna matching network requirements* of the component, the matching network is a  $\Pi$ -network. It consists of three components in a  $\Pi$ -configuration: one shunt  $C_{11}$ , then one in series  $L_5$ , and finally another shunt  $C_{12}$  (See schematic in Appendix). The optimum differential impedance at 2.4 GHz seen into the matching network from pin ANT1 and ANT2 on the QFN48 package is  $(15 + j85)\ \Omega$ , which is obtained following the *Antenna tuning* document, provided by the Nordic Semiconductor company, with  $C_{11} = 0.8\ \text{pF}$ ,  $L_5 = 3.3\ \text{nH}$  and  $C_{12} = 1.5\ \text{pF}$ . Finally a 2.4 GHz multilayer chip antenna (Wurth Elektronik) provides the Bluetooth transmission with an average gain of  $-0.5\ \text{dBi}$  and an omnidirectional radiation pattern. Figure 6.33 shows the PCB, which was designed respecting the following requirements:

- a double layer PCB with a widespread ground plane for both layers;
- a ground plane clearance around the antenna area (following the antenna datasheets constraints);
- only one layer of components to ensure a flat bottom surface;
- a round shape with a  $\varnothing < 45\ \text{mm}$ , compliant with the standard size of the ECG electrodes, used as mechanical support;
- a hole in the middle of the PCB provides a mechanical connection between the sensor and the ECG electrodes, through a metallic snap button.

### B. Firmware Design

The following paragraph describes in depth the logic adopted to compute the frequency of the signal coming as input in the system. The firmware encodes the frequency oscillation of the VCO signal ( $V_{VCO}$ ) and transmits the data via Bluetooth. More precisely, a General Purpose Input Output pin as input pin was used and the MCU was set to trigger an interrupt every time a rising edge is seen on the input pin. In addition, a 16 bit internal timer has been taken into account to keep track of the sampling rate of the signal. In terms of software, the mBed library for the nRF51822 has been chosen. The Nordic timer is configured so to execute a really small piece of code which increments the value of a counter variable every  $10\ \mu\text{s}$ . When the MCU sees the first rising edge it sets the counter variable to zero whereas, when the MCU sees the second rising edge, it computes the time

delta, in terms of samples, and it transforms the result in Hz according to the formula below:

$$f = \frac{1}{(nCounts \cdot sample\ rate)} \quad (6.16)$$

where  $f$  is the frequency and  $nCounts$  the number of counts. The code reported below initiates the system by creating the timer object, configuring the pin 23 as an interrupt input pin, setting the  $tCount$  variable to zero and finally the setting the  $seenRisingEdge$  to zero meaning that no rising edges are seen yet. Finally, the code starts the timer and register the input pin with the interrupt handler.

```
Ticker ticker;                                /* The timer object.
InterruptIn extSignal(p23);                   /* The signal to sample
/* comes to the pin 23.
static volatile uint32_t tCount = 0;          /* Samples counter.
static volatile uint8_t seenRisingEdge = 0; /* Set to 1 when a rising
/* edge is seen.

extSignal.rise(&signalDidRiseEdge);

ticker.attach_us(periodicCallback, SAMPLE_RATE_IN_us);
```

The code of the "periodicCallback" function is hereby reported.

```
void periodicCallback(void)
{
    tCount++;
}
```

As the reader may notice, the function increments the  $tCount$  variable and returns the program flow to the caller. As above mentioned, when a rising edge is seen on the input signal pin, an interrupt is fired. The MCU handles such an interrupt by executing the code below:

```
void signalDidRiseEdge(void)
{
    if(seenRisingEdge==1) {
        /* period is a global variable */
        period = tCount * SAMPLE_RATE_IN_us;
    }
    tCount = 0;
    seenRisingEdge = !seenRisingEdge;
}
```

The code above computes the signal period only when a rising edge of the input signal was recorded. If no rising edges were recorded, it just sets to zero the  $tCount$  variable. The period of the signal is later converted into a frequency and written to the Bluetooth Characteristic of the MCU that

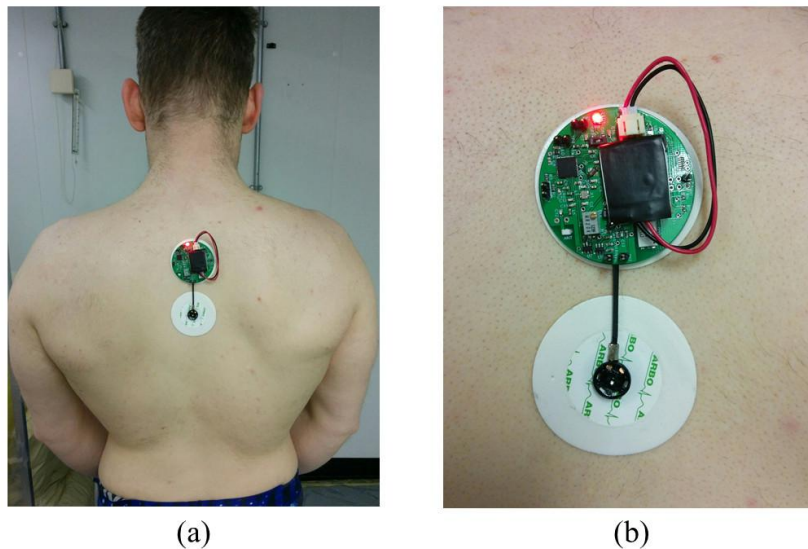


FIGURE 6.34: SEM system preliminary test.

emulates a UART port. Finally, the code below performs the BLE write.

```
void signalDidRiseEdge(void)
void writeToBLE(const uint8_t *data) {

    if (data!=NULL && uartServicePtr!=NULL) {
        uint16_t dataSize = strlen((char*) data);
        ble.updateCharacteristicValue(uartServicePtr->
            getRXCharacteristicHandle(), data, dataSize);
    }
}
```

### C. Implementation

Figure 6.34 depicts the final implementation of the SEM system coupled with the stretch sensor and the ECG electrodes. During the positioning step, the sensor was pre-stretched in order to enhance the stretching-relaxing hysteresis, as explained in Paragraph 6.5.3. Two custom "hooks" provide a robust connection of the sensor with the system, since the movements of the subject and the low stiffness of the skin can affect the mechanical stability of the device and the signal quality. A small LiPo battery (3.6 V 120 mAh) powers the system and it is placed on the top of the PCB.

## 6.6.5 Test and Results

### A. Preliminary Tests

Preliminary tests of the overall system were performed placing between T1-T3 vertebrae (Figure 6.34) and testing the BLE and IR-UWB communication. The tests reported in Light-of-Sight (LoS) propagation of a maximum

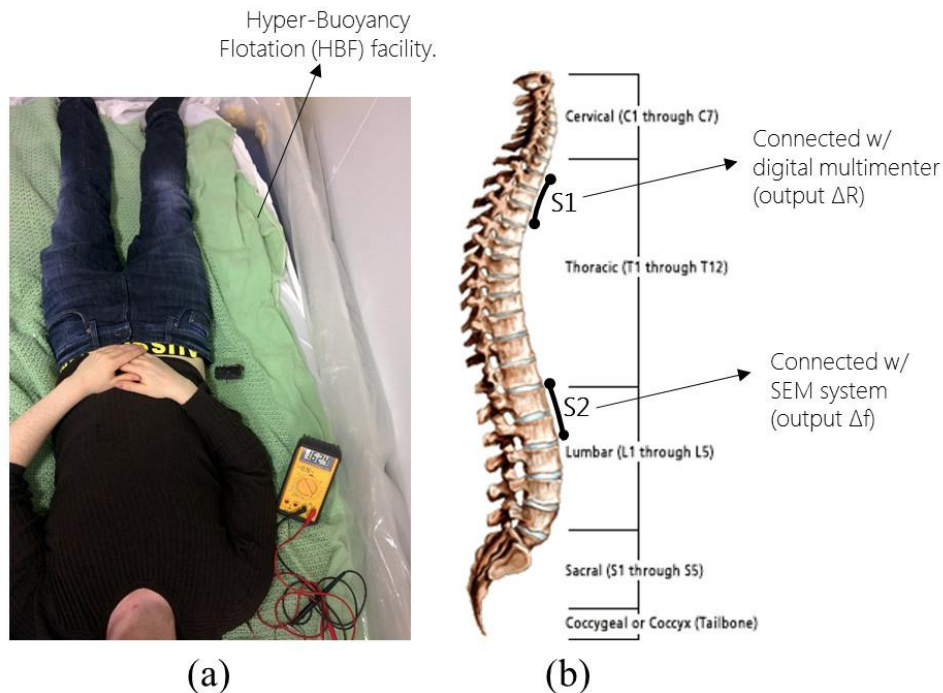


FIGURE 6.35: Placement of the S1 and S2 stretch sensors.

range of 15 m and 1 m using the BLE and UWB modules, respectively. As BLE receiver was used a smartphone using the Received Signal Strength Indication (RSSI) with the dedicated mobile App. The UWB receiver (RX) presented in Chapter 4 was used to evaluate the maximum transmission distance considering the Pulse Error Rate. In terms of power consumption in transmission mode, the BLE SoC consumes 50 mW w.r.t. to the 15 mW of the IR-UWB IC (in agreement with the results presented in Chapter 3). The Read-Out Circuit (ROC) was identical for both communication systems, reporting a power consumption of about 8 mW. These preliminary tests allowed also to validate the robustness of the SEM system after movements of the subject such as flexion, hyperextension, lateral flexion and rotation of the torso. No disconnection was observed during any movement.

### B. Spinal Elongation Experiment

The elongation of the spine was simulated with the Hyper-Buoyancy Flotation (HBF) facility. It was designed and implemented at King's College London (KCL). It comprises a hypersaline-filled water-bed developed to simulate a short term high fidelity model of spinal unloading. It allows to investigate the pathophysiology and develop techniques to ameliorate microgravity induced spinal elongation and associated back pain. In accordance with past tests, 4 hr of HBF experiment recorded an stature elongation of  $\sim 18\text{ mm}$  due to the increase of the intervertebral disc "height" during spinal unloading. In a single subject trial, the SEM device was set in

Bluetooth streaming mode, in order to be compliant with the receiver devices within the KCL facility. The SEM system was used for 5 hours of HBF experiment subdivided into three steps:

1. 4h 45' lying on the HBF facility (interrupted with a break of 10 min);
2. 10' sitting on a chair;
3. 15' lying on a normal bed.

This protocol was chosen in preparation for the next 8 hr HBF experiment followed by a MRI scan, in order to evaluate the structures of the spine precisely. For this reason, it also is relevant to investigate the behaviour of the spine during the carriage of the subject between the HBF facility to the hospital imaging department.

The stretch sensors, placed on the back of the subject, were pre-stretched of the 10% of the nominal length. The thoracic sensor was connected with a digital multimeter, to measure the resistance change, and the lumbar sensor was connected with the SEM system. Finally, the ( $\Delta R_{sens}$  and  $\Delta f_{osc}$ ) were converted into a length change of the selective spine portions. Elongation of the spine region and thus stretch of the sensor, causes an increasing in its electrical resistance and a decreasing the frequency of the ROC signal output.

Figure 6.36 (a) shows the mean resistance variation of the thorax sensor every 15 min. The same procedure was used with the lumbar sensor, calculating an average of 100 samples within a measurement window of 10 sec every 15 min. The Figure 6.36 (b) plots the mean frequency of the signal. Both graphs present a subdivision into the different phases of the experiment, and in detail:

- *phase (A)* – lying prone on the HBF;
- *phase (B)* – rising from the HBF and standing up;
- *phase (C)* - returning to the lying down on the HBF;
- *phase (D)* – sitting on a chair with back at 90°;
- *phase (E)* – lying down on the bed.

In terms of elongation, the expected results are a constant increase of the resistance and a constant decrease of the signal frequency, respectively, specially during *phase (A)*, *phase (C)* and *phase (E)*. Figure 6.36 (a) shows an complete opposite behaviour with a gradual decrease of the resistance, thus technically, a compression of the sensor, followed by a rapid increase when the subject stood up (*phase (B)*). Then, after the break, the phase

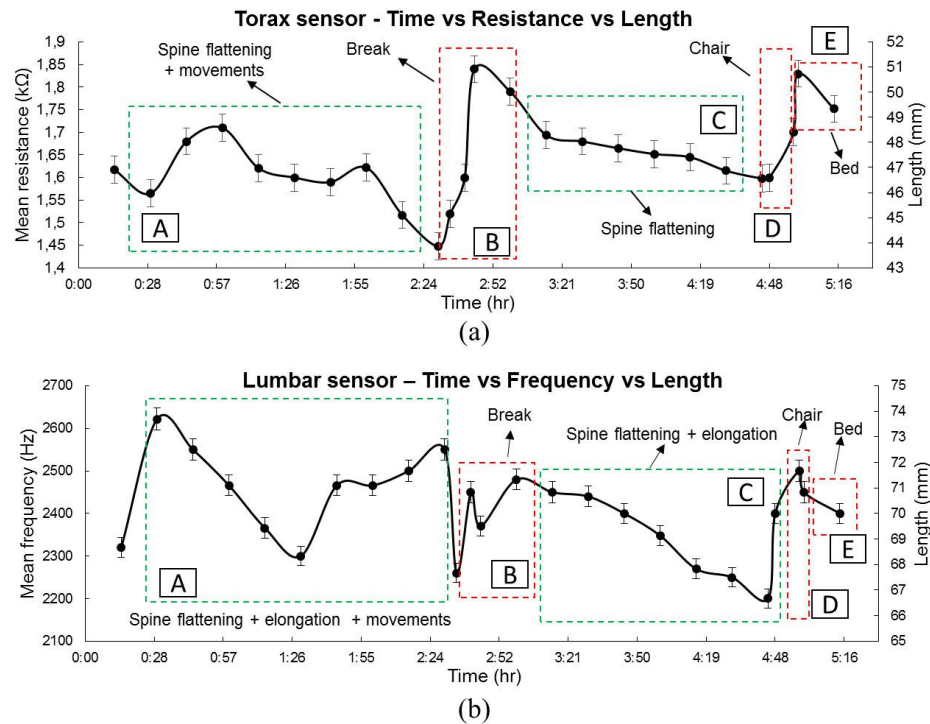


FIGURE 6.36: SEM system results after 5hr floitation test. (a) Resistance variation and (b) frequency variation with the spinal elongation.

(C) presents the same trend, up to the phase (D). The reason of these controversial results are due to the “spine flattening” process during the first part of the experiment. The kyphosis curvature tends to reduce its radius of curvature during the experiment. The sensor, previously stretched and positioned on the apex of kyphosis, begins to reduce its length during the “elongation phases” of the experiment. In that region of the spine, the intervertebral distance is less than the lumbar portion, therefore the contribution of the elongation mainly comes from the “spine flattening”, rather than from the increase of the intervertebral disc “height”. A smoothness decrease of the resistance has been recorded when the subject slept (phase (C)), unlike the phase (A) that it is affected by motion artefacts. The thorax sensor, attached on the back with the subject in lying down position, measured a maximum displacement of 5 mm.

Figure 6.36 (b) depicts the results of the lumbar sensor in which, motion artefacts aside, shown an expected trend with a gradual increase of the sensor length during phase (A), (C) and (E). Opposite tendency during phase (B) and (D) when the subject stood up. Observing the graph, the transition between the A – B and the C – D phases was very quick and the spine tried to return slowly to the original condition. Likewise with the lumbar sensor, a slight “spine flattening” was observed coupled with an increase of

the intervertebral spacing, since the sensor was placed just over the peak of the spine curvature. The amount of the stretch recorded was around 7 mm.

### 6.6.6 Conclusion

In this Chapter, the first wearable and no invasive device able to measure selectively elongation of the spine (Spinal Elongation Monitoring system) has been presented. The device was developed with a stretchable piezo-resistive material coupled with a custom electronic circuit directly attached on the body of the subject. Two different short-range and low power consumption wireless technologies were implemented within the same system, with the opportunity to switch between them. BLE and IR-UWB short-range technologies were selected for their compact chipset (QFN package), low power consumption, short list of extra components and simple interface with the relative receivers. The results of the preliminary tests demonstrated the efficiency of the system of both wireless module with a wider range of transmission with the BLE (15 m) and a lower power consumption obtained with the IR-UWB (15 mW (TX)). Then, the mechanical robustness of the overall system was tested considering the issues due to movements and the soft and uneven surface of the back. The results of the experiments allowed to study the behaviour of the spine during unloading, showing that the elongation may occurs in the lumbar area where anatomically the nominal height of the vertebrae and intervertebral discs are higher than the thorax area. In both cases, it seems that the elongation was preceded by a flattening phenomenon which was prevalent observed on the thorax area, given that the sensor was placed at the apex of the kyphosis curvature. The sensor, pre-stretched during the experiment preparation, measured a untrue "compression" of the spine during the experiment session due to the flattening phenomenon. Finally, during the phase (*D*) and (*E*) of the experiment, the length of the spine changed rapidly mainly due to the recover of the anatomical curves of the back.

The SEM system had demonstrated the chance to monitor the behaviour of the spine during unloading selectively, providing a scientific support for the next steps of the research activities which will include a MRI analysis and a long-term bed-rest experiments with and without the GLCS.

## Chapter 7

# Conclusion

In this thesis work, a scientific contribution for the next generation of wearable technologies were presented, with a particular focus on circuit design of ultra-low power wireless technologies, the realization of smart piezoresistive / piezocapacitive and electro-active material, the design of read-out circuits and system integration/implementation. The research activities were carried out following an "application driven" approach, addressing the diverse challenges with a multidisciplinary method. This thesis begins with the establishment of the research area. Due to the interdisciplinary nature of the research topic, general requirements and challenges were presented, then the following chapters were structured with: I) a dedicated introduction in order to figure out the challenge to address, II) the solution proposed, III) characterization/tests, IV) experimental results and V) conclusions and discussion of the results.

In Chapter 2, the first objective was to combine a smart sensor, based on a piezo-capacitive polymer, and a custom read-out circuit within a fabric substrate. The transducer and the circuit were designed, developed and characterized in order to be compliant with the project requirements. The result was a compact and fully integrated sensor system, able to identify a contact event with a pressure resolution of 10 kPa and, at the same time, able to measure a pressure variation up to 4 MPa. The touch-pressure characteristics, the small design of the ROC, placed directly beneath the transducer, and the final fabric integration represents a novel contribution with respect to the similar commercial, bulky and stand alone pressure and/or touch systems.

In terms of short-range ultra-low power wireless communication systems for wearable technologies, in Chapter 3 a novel IR-UWB systems was presented. Requirements, challenges and current solutions among the wearable WBAN devices, mainly based on Bluetooth technology, were introduced. The IR-UWB (TX/RX) proof-of-concept designed and developed was able to demonstrate the streaming of a complex signal, such as an audio signal, with a radio range of 2.5 m and with a very low power consumption, equal to 7.52 mW (TX) and 32.4 mW (RX) respectively. The results allowed

to prove the effectiveness of the IR-UWB as a real wireless technology alternative for the next generation of wearable WBAN devices.

In Chapter 4, the IR-UWB was used to develop a low-complexity ultra-low power Face-to-Face detector and, at the same time, a proximity sensor. Current solutions were introduced pointing out the high power consumption of the technology used, the presence of an external infrastructure, the proximity techniques adopted and the overall size. The final objective was to monitor the Doctor-Patient interaction during the hospitalization with relevant interest also about the human proximity. The final application is aimed to a deep investigation of the infections spreading behaviour within the hospital community. A proof-of-concept was designed and developed exploiting the IR-UWB with a Pulse-Error-Rate approach to evaluate the TX-RX distance. The TX-RX system proposed was able to detect the Doctor-Patient interaction with a range of 50 cm and to measure the relative distance with a 2-D spatial accuracy of 3 cm. The information was streamed to a graphical user interface able to count the number of interactions and to show the proximity. The transmitter, connected with a portable device (e.g. smartphone), or with further improvements in the stand alone configuration, consumed 10.8 mW with an autonomy of 8 h with a 120 mAh rechargeable battery.

In terms of wearable actuators, a novel contribution for the next generation was discussed in Chapter 5. ElectroActive Polymers, and in particular Dielectric Elastomers, are representative of a class of smart materials that are able to produce a deformation by applying a voltage. This technology was introduced and the relative technological challenges were detailed. A new concept of EAP geometry inspired by the muscle architecture and a proof-of-concept of the EAP working principle based on dielectric elastomer was presented in this Chapter. A deep analysis of the EAP multilayer configuration, well known among the scientist community, in addition to the application of different voltages for each layer, led to relevant improvements within the soft actuator technology. A fine control of the deformation and lower driving voltage were part of these improvements with respect to the literature. Since an excessive increase in the number of layers can lead to a stiffening of the actuator, the coaxial geometry aimed to solve this issue. Increasing the surface area of the electrodes, a performance improvement was obtained without affecting the mechanical properties of the material. Furthermore, a coaxial structure allowed to develop active fibers, which can be potentially woven within a fabric, filling the gap of the wearable man-machine interface. This solution was patented and brought to a further level of innovation, taking inspiration from the natural muscle

anatomy. In principle, a multi-fibers coaxial configuration would allow a further improvement of the EAP fibers performance, introducing the possibility to control the strength and movement of the fiber with a selective activation of the fibers, as it happens in muscle fibers.

In the end, in Chapter 6 it is represented a scientific collector of the previous experiences within the wearable technology field. The research activities carried on within the Gravity Load Countermeasure Skinsuit (GLCS) project had the objective to turn the SkinSuit from a passive into an active wearable countermeasures system and to monitor the effects of the microgravity on the spinal column, by means of a novel wearable device. An explanation of the background of the physiological effects on the human body due to the space environment and the State Of the Art (SoA) of the current countermeasures was presented.

The first solution proposed was a Gz-load adjustment mechanism designed to change the stretch level of the SkinSuit. The overall mechanism was developed, tested and characterized with an ad-hoc GLCS simulator.

Then, in order to monitor the Gz-load variation, the first approach was to use a force sensor placed beneath the feet and integrated with the SkinSuit stirrups (Load Monitoring System). The Force Sensing Resistor (FSR) technology was selected as the best force sensor candidate in terms of force range, sensitivity, geometry and simple integration with the wearable system. The sensor was then characterized before the final integration, showing a sensing behaviour compliant with the project requirements. Then, the sensor coupled with a read-out circuit, was tested with the GLCS simulator. The results were unreliable with a poor repeatability, mainly due to the anatomy of the foot, to the flexibility of the stirrup and to the slight movements of the sensor.

These results led to consider another approach, exploiting the elastic properties of the SkinSuit and using a wearable stretch sensor (Stretch Monitoring System). The Mark V SkinSuit was characterized in terms of *stretch*–*Gz*-load variation in order to select the right placement of the stretch sensor. After a technical benchmark of the commercially available solutions, a custom stretch sensor based on a piezo-resistive polymeric material was developed and characterized. The sensor, connected with a read-out circuit based on a Schmitt trigger oscillator, was able to generate a quasi-digital signal, shifting the frequency of the square wave in response to a deformation of the sensor. The information was processed and transmitted via Bluetooth to a custom user interface. The sensor was embedded within the Mark V SkinSuit using conductive threads in order to fix it in position and to connect the sensor with the electronic module. Finally, the overall system was tested with different Gz-loads and the results presented an almost

linear stretch behaviour, both in resistance and frequency variation with different static loads.

In the end, the first wearable and not invasive device able to measure selectively elongation of the spine (Spinal Elongation Monitoring system) was presented. The device consists of a stretchable piezo-resistive material coupled with a custom electronic circuit directly attached on the body of the subject. The circuit was able to encode the length change of the sensor into a frequency shift through a ROC based on a VCO. Then, BLE and IR-UWB technologies were both selected for short-range and low power consumption wireless communication and implemented within the circuit. This allowed to compare directly both technologies in terms of performance and energy efficiency, to interface the device with an existing wireless system using BLE and to set the device for the next generation of wearable wireless technology through the IR-UWB. The results of preliminary tests demonstrated the efficiency of both wireless module with a wider range of transmission with the BLE (15 m) and a lower power consumption obtained with the IR-UWB (15 mW (TX)). From the point of the sensing material, a new piezo-resistive stretch sensor was developed and compared with previous ones. The mechanical robustness of the overall system was tested considering the issues raising from the movements and the soft and uneven surface of the back. The results of the experiments allowed to study the behaviour of the spine unloading condition, showing that the presumably most likely elongation occurs mainly in the lumbar area (7 mm) in which, anatomically, the nominal height of vertebrae and intervertebral discs is higher than in the thorax area (5 mm). In both cases, the elongation was preceded by a flattening phenomenon which was mainly observed on the thorax area, given that the sensor was placed at the apex of the kyphosis curvature. In fact, the sensor, pre-stretched during the experimental set up, measured a false "compression" of the spine during the experiment due to the flattening phenomenon. The device performed continuously for 5 h saving the measurements every 15 min. This last scientific contribution allowed to collect together the competences, knowledge and results of the previous activities by designing, developing and testing on field a new wearable devices.

As a final consideration, the vision of wearable computing describes future electronic systems as an integral part of our "everyday clothing", serving as intelligent personal assistants. Therefore, such wearable sensors must maintain their sensing capabilities under the demands of normal clothes, which can impose severe mechanical deformation of the underlying garment, fabric substrate or human skin. The potential applications are several and wearable technologies have a direct link with human body monitoring. "Clothes are our own personal house" (Van Langenhove et al.,

2007) and there is no other device continuously in contact with the human body like garments. This way, the combination of smart materials, wearable electronics, low-power wireless technologies, sensors and the systems integration within a fabric or a human body, must be put together to understand the new generation of wearable devices. Textiles and clothes can be produced on fast and productive machinery at a reasonable cost, and the health and beauty industry is also taking advantage of these innovations.

Finally, the vision behind the current and near-future wearable technology, like in this thesis, is based on a highly multidisciplinary approach with an objective aimed at the final application, addressing and solving manifold challenges.